Chapter 6

What triggers starbursts in low-mass galaxies?

— **Federico Lelli, Marc Verheijen, and Filippo Fraternali** —

In preparation for submission to MNRAS

Abstract

Strong bursts of star-formation in galaxies may be triggered either by internal or external mechanisms. We study the large-scale H I emission in 18 nearby starbursting dwarfs, that have accurate star-formation histories from HST observations. We found that these objects show a broad, continuous range of H I morphologies. Several galaxies have heavily disturbed H I morphologies, with major asymmetries, long filaments, and/or severe offsets between the H I and stellar distributions, whereas other galaxies show only minor asymmetries in their outer regions. We quantify these asymmetries for both our sample and a control-sample of non-starbursting dwarf irregulars, drawn from the VLA-ANGST survey. Starbursting dwarfs appear to have more asymmetric H I morphologies than typical irregulars, suggesting that some external mechanism triggered the intense star-formation. Moreover, galaxies hosting an old burst ($\gtrsim$100 Myr) have more symmetric H I morphologies than galaxies hosting a young one ($\lesssim$100 Myr), indicating that the former ones probably had enough time to regularize their outer H I distribution since the onset of the burst. These results suggest that the starburst is triggered by interactions/mergers between gas-rich dwarfs and/or by direct gas infall from the IGM.

6.1 Introduction

The mechanisms that trigger strong bursts of star-formation in low-mass galaxies are poorly understood. Unlike spiral galaxies, gas-rich dwarfs usually do not have strong density waves and stellar bars, thus internal mechanisms such as bar-driven gas inflows are generally ruled out (e.g. Hunter & Elmegreen 2004). Other internal mechanisms, however, have been proposed, like torques due to massive star-forming clumps (Elmegreen et al. 2012), triaxial dark matter haloes (Bekki & Freeman 2002), or bars made of dark matter (Hunter & Elmegreen 2004). External mechanisms are also possible, like tidal perturbations from nearby companions (e.g. Noguchi 1988), interactions/mergers between gas-rich dwarfs (e.g. Bekki 2008), or cold gas accretion from the IGM (e.g. Silk et al. 1987). In particular, cosmological models predict that low-mass galaxies should accreate most of their gas through cold flows, reaching the central parts of the dark matter halo without being shock-heated to the virial temperature (e.g. Dekel & Birnboim 2006). This process may still take place at $z \simeq 0$ in low-density environments (Kereš et al. 2005), thus isolated starbursting dwarfs in the nearby Universe are prime locations to search for cold gas accretion.

In Chapter 4, we studied the H I content of 18 starbursting dwarfs (hereafter blue compact dwarfs, BCDs) and found that complex H I kinematics are much more common in BCDs ($\sim$50%) than in typical irregulars ($\sim$10%). This may be related to the starburst trigger (interactions/mergers or disk instabilities), but may also be a consequence of feedback from supernovae and stellar winds, making it difficult to distinguish between different triggering mechanisms. The other $\sim$50% of BCDs, instead, have a regularly-rotating H I disk, which can be used to derive rotation curves and investigate the internal distribution of mass. In Chapter 5, we found that BCDs generally have steeper rotation curves than typical irregulars (Irrs) of the same total mass (see also van Zee et al. 2001), suggesting that there is a close link between the starburst activity and the shape of the gravitational potential. A central concentration of mass (gas, stars, and dark matter) seems to be a characterizing property of BCDs and must be tightly linked to the mechanism that triggers the starburst.

Environmental studies can also provide important clues about the triggering mechanism. BCDs tend to populate low-density environments (e.g. Iovino et al. 1988; Salzer 1989; Telles & Maddox 2000; Lee et al. 2000) and are not necessarily associated with *bright* galaxies (e.g. Campos-Aguilar & Moles 1991; Campos-Aguilar et al. 1993; Telles & Terlevich 1995; Pustilnik et al. 1995), suggesting that tidal interactions with *massive* companions are *not* a dominant starburst trigger. The possibility of interactions with low-luminosity, low-surface-brightness (LSB) galaxies, however, remains open (e.g. Méndez et al. 1999; Méndez & Esteban 2000; Noeske et al. 2001; Pustilnik et al. 2001b), given that these objects are usually under-represented in optical catalogs. Moreover, if the starburst is due to a *past* interaction/merger with a LSB dwarf, the resulting tidal features would have very low surface brightnesses and be difficult

Table 6.1 – Galaxy Sample

Name	Alternative Name	R.A. (J2000)	Dec. (J2000)	$V_{\rm sys}$ – (km s^{-1}) –	$V_{\rm rot}$	Dist (Mpc)	$M_{\rm R}$ (mag)	$R_{\rm opt}$ (kpc)	12+log(O/H)	Ref.
NGC 625	ESO 297-G005	01 35 04.3	-41 26 15	398±6	30±5	3.9±0.4	-17.25±0.24	3.3	8.08±0.12	a, g, l
NGC 1569	UGC 3056	04 30 49.0	+64 50 53	-80±10	50±5	3.4±0.2	-17.14±0.25	3.0	8.19±0.02	a, h, m
NGC 1705	ESO 158-G013	04 54 13.9	-53 21 25	635±2	72±10	5.1±0.6	-16.35±0.26	1.5	8.21±0.05	b, i, l
NGC 2366	UGC 3851	07 28 51.9	+69 12 34	103±1	49±6	3.2±0.4	-16.64±0.27	4.4	7.91±0.05	a, h, l
NGC 4068	UGC 7047	12 04 02.7	+52 35 28	206±2	39±5	4.3±0.1	-15.67±0.05	1.8	...	a, h
NGC 4163	UGC 7199	12 12 09.0	+36 10 11	158±4	10±5	3.0±0.1	-14.81±0.10	1.0	7.56±0.14	a, h, l
NGC 4214	UGC 7278	12 15 38.8	+36 19 39	291±1	81±9	2.7±0.2	-17.77±0.24	2.2	8.22±0.05	a, h, l
NGC 4449	UGC 7592	12 28 10.8	+44 05 37	210±5	35±5	4.2±0.5	-18.88±0.26	3.3	8.26±0.09	a, h, l
NGC 5253	Haro 10	13 39 56.0	-31 38 31	410±10	...	3.5±0.4	-17.61±0.27	2.1	8.12±0.05	a, g, k
NGC 6789	UGC 11425	19 16 41.9	+63 58 17	-151±2	57±9	3.6±0.2	-15.09±0.14	0.7	...	a, i
UGC 4483	...	08 37 03.4	+69 46 31	158±2	19±2	3.2±0.2	-12.97±0.19	0.6	7.56±0.03	a, i, l
UGC 6456	VII Zw 403	11 27 57.2	+78 59 48	-102±4	10±5	4.3±0.1	-14.41±0.05	1.2	7.69±0.01	a, j, n
UGC 6541	Mrk 178	11 33 28.9	+49 14 22	250±2	...	4.2±0.2	-14.61±0.10	0.9	7.82±0.06	c, j, l
UGC 9128	DDO 187	14 15 56.8	+23 03 22	150±3	24±4	2.2±0.1	-12.82±0.12	0.6	7.75±0.05	a, h, l
UGCA 290	Arp 211	12 37 22.1	+38 44 41	468±5	...	6.7±0.4	-14.09±0.18	0.9	...	d, i
I Zw 18	Mrk 116	09 34 02.0	+55 14 25	767±4	38±4	18.2±1.4	-14.99±0.26	0.5	7.20±0.01	e, j, k
I Zw 36	Mrk 209	12 26 16.8	+48 29 39	277±2	29±2	5.9±0.5	-14.88±0.23	0.9	7.77±0.01	f, i, k
SBS 1415+437	...	14 17 02.1	+43 30 19	616±2	18±2	13.6±1.4	-15.90±0.25	2.4	7.62±0.03	a, i, o

Notes. The values of the center are derived from R-band or V-band images; the rotation velocities $V_{\rm rot}$ are measured at the outermost radii accessible by H I data at relatively-high spatial resolutions (see Chapter 4 for details). Distances are derived from the tip of the red giant branch. The optical radius $R_{\rm opt}$ is defined as 3.2 exponential scale-lengths. The last column provides references for the distance, the integrated photometry, and the ionized gas metallicity, respectively.

References. (a) McQuinn et al. (2010); (b) Annibali et al. (2003); (c) Schulte-Ladbeck et al. (2000); (d) Crone et al. (2002); (e) Annibali et al. (2013); (f) Schulte-Ladbeck et al. (2001); (g) Lauberts & Valentijn (1989); (h) Swaters & Balcells (2002); (i) Gil de Paz et al. (2003); (j) Papaderos et al. (2002); (k) Izotov & Thuan (1999); (l) Berg et al. (2012); (m) Kobulnicky & Skillman (1997); (n) Thuan & Izotov (2005); (o) Guseva et al. (2003).

to unambiguosly identify, unless very deep optical imaging is available (e.g. López-Sánchez 2010; Martínez-Delgado et al. 2012).

Alternatively, deep 21 cm-line observations can be used to search for gas-rich companions, infalling gas, or signatures of past interactions/mergers (e.g. Sancisi et al. 2008). Taylor et al. (1993, 1995, 1996) obtained low-resolution *Very Large Array* (VLA) observations of 21 BCDs and 17 LSB Irrs, and concluded that BCDs have nearby "H I companions" more than twice as often as LSB Irrs, highlighting the possible importance of low-mass perturbers. Studies of the large-scale H I emission in individual objects have revealed that several BCDs show extended and filamentary H I structures, which may indicate either a recent interaction/merger or cold gas accretion from the environment; e.g. NGC 1569 (Stil & Israel 2002), IC 10 (Manthey & Oosterloo 2008), and NGC 5253 (López-Sánchez et al. 2012). In some cases, the presence of a nearby companion and/or stellar tidal features clearly points to an interaction/merger between gas-rich dwarfs; e.g. II Zw 40 (van Zee et al. 1998), II Zw 70/71 (Cox et al. 2001), and I Zw 18 (Lelli et al. 2012a). However, some BCDs seem to have relatively-symmetric and unperturbed H I disks, undermining the importance of external mechanisms in triggering the starburst; e.g. NGC 2915 (Elson et al. 2011) and VII Zw 403 (Simpson et al. 2011). The relative fraction of BCDs with extended symmetric/asymmetric H I morphologies in their outer regions is unclear, as well as the detailed relation between the extended H I emission and the starburst activity.

Here we present a detailed and systematic study of the large-scale H I emission in 18 starbursting dwarfs. The properties of our sample have been described in Chapter 4, and are summarized in Tables 6.1 and 6.2. In particular, the information provided by the star formation histories (SFHs) of these galaxies allows us to compare the starburst timescales with the dynamical timescales in the outer parts, and investigate the possible relation between the H I morphology and the starburst activity.

6.2 Data analysis

For the 18 galaxies in our sample, we collected both new and archival 21 cm-line observations. The collection and reduction of these observations are described in detail in Chapter 4, where we presented H I data at relatively-high spatial resolutions (ranging from 5″ to 30″ depending on the individual galaxy properties). Here we present H I data at lower spatial resolutions, which are more sensitive to the diffuse H I emission on large scales. We use the same dataset as in Chapter 4 except for two objects: NGC 4449 and UGC 4483. For NGC 4449, the H I datacube from THINGS (Walter et al. 2008) covers a relatively small region on the sky, thus we consider here the total H I map and velocity field from Hunter et al. (1998), which were obtained from VLA D-array observations in a 3×3 pointing mosaic (covering ∼1°). For UGC 4483,

Table 6.2 – Properties of the starburst.

Galaxy	b	SFR_0	SFR_p	$\Sigma_{SFR}(0)$	$\Sigma_{SFR}(t_p)$	$\log(sSFR_0)$	$\log(sSFR_p)$	t_p	Ref.
		($10^{-3}M_\odot$	yr^{-1})	($10^{-3}M_\odot$ yr^{-1}	kpc^{-2})	—— (Gyr^{-1}) ——		Myr	
NGC 625	3.0±0.1	4±2	86±20	0.12±0.06	2.5±0.6	-2.66±0.63	-1.33±0.45	820±180	a
NGC 1569	21±1	80±15	240±10	2.8±0.5	8.5±0.3	-1.79±0.21	-1.31±0.11	40±10	a
NGC 1705	∼6	314±78	314±78	44±11	44±11	-0.65±0.56	-0.65±0.56	3.0±1.5	b
NGC 2366	5.6±0.4	43±9	160±10	0.7±0.1	2.6±0.2	-1.63±0.24	-1.06±0.13	450±50	a
NGC 4068	4.7±0.3	31±7	42±3	3.0±0.7	4.5±0.3	-1.70±0.26	-1.56±0.15	360±40	a
NGC 4163	2.9±0.6	5.2±1.6	12±3	1.6±0.5	3.8±0.9	-2.13±0.43	-1.77±0.39	450±50	a
NGC 4214	3.1±0.9	64±13	130±40	4.2±0.8	8.5±2.6	-1.49±0.32	-1.18±0.40	450±50	a
NGC 4449	6.0±0.5	970±70	970±70	28±2	28±2	-1.18±0.18	-1.18±0.18	5±3	a
NGC 5253	9.0±0.9	162±13	400±40	12±0.9	29±3	-1.82±0.16	-1.43±0.17	450±50	a
NGC 6789	3.8±1.3	3.0±1.3	15±5	1.9±0.8	9.7±3.2	-2.21±0.52	-1.51±0.44	565±65	a
UGC 4483	14±3	11±4	11±2	9.7±1.8	8.8±3.5	-0.80±0.27	-0.84±0.45	565±65	a
UGC 6456	7.6±1.1	23±3	23±3	5.1±0.7	5.1±0.7	-1.18±0.42	-1.18±0.42	16±8	a
UGC 6541	∼3	3.0±1.5	...	1.2±0.6	...	-1.27±0.71	...	...	c
UGC 9128	6.3±1.4	0.7±0.4	5±1	0.6±0.3	4.4±0.9	-2.11±0.59	-1.26±0.25	150±50	a
UGCA 290	∼3	11±8	42±15	4.3±3.1	16±6	-0.80±0.88	-0.22±0.61	15±5	d
I Zw 18	∼30	100±50	100±50	127±64	127±64	-0.07±0.73	-0.07±0.73	10±5	e
I Zw 36	∼7	25±12	...	9.8±4.7	...	-0.35±0.69	...	...	f
SBS 1415+437	∼12	40±7	150±10	2.2±0.4	8.3±0.5	-1.47±0.25	-0.90±0.19	450±50	a

Notes. For a detailed description of these quantities, see Sect. 6.4.3. For NGC 1705, UGC 6541, UGCA 290, I Zw 18, I Zw 36, and SBS 1415+437, the SFH at ages $\gtrsim$1 Gyr is uncertain due to the relatively-shallow photometric dept of the color-magnitude diagrams ($\lesssim$1 mag below the tip of the red giant branch), thus the values of b, $sSFR_0$, and $sSFR_p$ are approximate. The most problematic case is I Zw 18, where we prefer to use the SFR derived from Hα observations (Chapter 5) rather than the value derived from fitting the CMD.

References. (a) McQuinn et al. (2010); (b) Annibali et al. (2003); (c) Schulte-Ladbeck et al. (2000); (d) Crone et al. (2002); (e) Annibali et al. (2013); (f) Schulte-Ladbeck et al. (2001).

in Chapter 3 (Lelli et al. 2012b) we reduced and analysed archival H I data obtained with the B- and C-arrays of the VLA, but here we analyse the datacube from Ott et al. (2012) that includes also new D-array observations, probing low-column-density gas on large angular scales.

For every galaxy, we chose the optimal spatial resolution using the following approach. We first inspected the H I cube at the highest spatial and spectral resolutions available. Then, this cube was progressively smoothed in the image plane to $10''$, $20''$, $30''$, and $40''$, and total H I maps at different spatial resolutions were constructed by summing masked channel maps. The smoothing procedure was halted when the total H I map reached a 3σ column density sensitivity of $\sim 10^{20}$ atoms cm^{-2}, which is adeguate to investigate the H I morphology on large-scales (e.g. Swaters et al. 2002) and, at the same time, allows us to preserve a relatively-high angular resolution (typically $20''$ except for 4 cases, see Table 6.3). The masks were obtained by smoothing the cube in velocity to $\sim$10 km s^{-1} and in the image plane to $1'$ ($2'$ for NGC 2366, NGC 4214, and NGC 5253 given their large angular extent), and clipping at $3\sigma_{1'}$ ($\sigma_{1'}$ is the rms noise in the smoothed cube). For NGC 4214, the cube was smoothed in velocity to only $\sim$2.6 km s^{-1} because only a few line-free channels were available at its high-velocity end. All the masks were visually inspected; residual noise peaks and Galactic emission were interactively blotted out. Note that the original, high-resolution cubes were obtained using a robust weighting technique (Briggs 1995) with robust parameter $\Re \simeq 0$, thus they have relatively-low column-density sensitivity, but their beam profile is close to a Gaussian shape. We avoided using natural-weighted datacubes because the broad wings of their beam profiles may lead to spurious detections of diffuse emission, especially when the H I data are not cleaned down to the noise level (as is the case for the LITTLE-THINGS datacubes that are cleaned down to only 2.5σ, see Hunter et al. 2012).

Since we are interested in the large-scale, diffuse H I emission, it is important to accurately estimate the 3σ column density sensitivity of the total H I maps. The noise in a total H I map is not uniform but varies from pixel to pixel because at each spatial position one adds a different number of channel maps, given that only the pixels inside a given mask are considered. Following Verheijen & Sancisi (2001), we constructed signal-to-noise maps and calculated a pseudo-3σ column density contour $N(3\sigma)$ by averaging the values of the pixels with signal-to-noise ratio between 2.75 and 3.25. We also calculated the rms of these pixels and used it to estimate the typical uncertainty on $N(3\sigma)$. In particular, we halted our smoothing procedure when the value of $N(3\sigma)$ was equal to 1×10^{20} cm^{-2} within the errors. The derivation of the signal-to-noise maps is described in detail in Appendix 6.A.

Total H I fluxes were calculated from the smoothed maps, by considering only the pixels with a flux density higher than $0.5 \times N(3\sigma)$, that can be considered as a pseudo-1.5σ contour. The H I fluxes are in overall agreement

Table 6.3 – Properties of the H I datacubes.

Galaxy	Telescope	Source	Smoothed Beam (asec×asec)	Smoothed Beam (pc×pc)	Ch. Sep. (km s^{-1})	Taper	Rms Noise (mJy/beam)	pseudo-$N(3\sigma)$ (10^{20} cm^{-2})	pseudo-$N(3\sigma)$ ($M_\odot$ pc^{-2})
NGC 625	VLA	a	30.0×30.0	567×567	2.6	Hann.	2.6	1.1±0.5	0.9±0.4
NGC 1569	VLA	b	20.0×20.0	330×330	2.6	Hann.	1.1	1.6±0.7	1.3±0.6
NGC 1705	ATCA	c	20.0×20.0	494×494	3.5	Hann.	1.2	1.1±0.4	0.9±0.3
NGC 2366	VLA	b	20.0×20.0	310×310	2.6	Hann.	1.3	1.5±0.6	1.2±0.5
NGC 4068	WSRT	d	30.0×30.0	625×625	2.0	Unif.	4.4	1.4±0.5	1.2±0.4
NGC 4163	VLA	b	20.0×20.0	290×290	1.3	Hann.	1.3	0.9±0.3	0.8±0.3
NGC 4214	VLA	b	30.0×30.0	393×393	1.3	Hann.	3.0	1.2±0.6	1.0±0.5
NGC 4449	VLA	e	62.0×54.0	1262×1099	5.2	Hann.	1.3	∼0.7	∼0.6
NGC 5253	ATCA	f	40.0×40.0	679×679	9.0	Unif.	2.7	1.0±0.3	0.8±0.3
NGC 6789	WSRT	a	20.0×20.0	349×349	2.0	Unif.	1.3	1.0±0.3	0.8±0.3
UGC 4483	VLA	g	20.0×20.0	310×310	2.6	Hann.	1.6	1.1±0.3	0.9±0.3
UGC 6456	VLA	a	20.0×20.0	417×417	2.6	Hann.	2.4	1.6±0.7	1.3±0.6
UGC 6541	VLA	b	20.0×20.0	408×408	1.3	Hann.	1.8	1.4±0.4	1.2±0.3
UGC 9128	VLA	b	20.0×20.0	213×213	2.6	Hann.	1.6	1.3±0.4	1.0±0.3
UGCA 290	VLA	a	20.0×20.0	650×650	1.6	Unif.	2.0	1.1±0.3	0.9±0.3
I Zw 18	VLA	h	20.0×20.0	1765×1765	1.3	Hann.	1.0	1.0±0.6	0.8±0.4
I Zw 36	VLA	b	20.0×20.0	572×572	2.6	Hann.	1.9	1.3±0.4	1.0±0.3
SBS 1415+437	VLA	a	20.0×20.0	1319×1319	1.6	Unif.	2.8	1.3±0.3	1.0±0.3

References. (a) Chapter 4; (b) Hunter et al. (2012); (c) Elson et al. (2013); (d)Swaters et al. (2002); (e) Hunter et al. (1998); (f) López-Sánchez et al. (2012); (g) Ott et al. (2012); (h) Lelli et al. (2012a).

with those from single-dish observations: the differences are typically $\lesssim$15%, apart for two objects (NGC 1569 and UGC 6456) that are affected by Galactic emission. Our smoothed H I maps, therefore, recover most of the H I emission from the galaxy.

We also derived H I velocity fields by estimating an intensity-weighted mean (IWM) velocity from the masked datacube at the optimal resolution, clipping at 2σ and considering only the pixels within the pseudo-3σ contour of the total H I map. Since the H I profiles are broad and asymmetric, these low-resolution IWM velocity fields are uncertain and provide only an overall description of kinematics of the extended gas. For the 18 galaxies in our sample, a detailed analysis of the H I kinematics has been presented in Chapter 2 (Lelli et al. 2012a), Chapter 3 (Lelli et al. 2012b), and Chapter 4, and we refer to these Chapters for details.

6.3 The large-scale H I emission

In the following, we discuss the overall properties of the diffuse H I emission in our sample of starbursting dwarfs, while in Sect. 6.5 we describe each individual galaxy in detail. In Sect. 6.4, we introduce the asymmetry parameter A, that quantifies the H I morphology in the outer regions; A is then used to make a comparison with a control-sample of typical irregulars (Irrs) and to investigate the possible relations between the large-scale H I distribution and the starburst.

Figs 6.1 and 6.2 show the total H I maps of our 18 galaxies superimposed on optical images; in each map the iso-density contours correspond to 1, 4, and 16×10^{20} atoms cm^{-2}. In Fig. 6.1 each box has a physical size of 20×20 kpc, while in Fig. 6.2 the sizes of the boxes have been optimized to appreciate the details of each individual object. It is clear that the diffuse H I emission in BCDs presents a large variety of sizes and morphologies. Several galaxies show heavily disturbed H I distributions, characterized by large-scale asymmetries, long filaments, and/or a severe optical-H I offset (e.g. NGC 1569, NGC 1705, NGC 4449, UGC 6541, UGCA 290, I Zw 18, and I Zw 36). Other galaxies, instead, show lopsided H I morphologies, characterized by minor asymmetries and/or extensions in the outer parts (e.g. NGC 2366, NGC 4068, NGC 4214, UGC 4483, UGC 6456, UGC 9128, and SBS 1415+437). There is *not* a clear-cut separation between these two types of H I morphologies, since there are several "intermediate" cases that have relatively-regular H I distributions in the inner parts and small tails/filaments in the outer regions (e.g. NGC 625, NGC 4163, NGC 5253, and NGC 6789).

We estimated the extent of the H I distribution $E_{\rm H\,I}$ by measuring the projected distance between the optical center of the galaxy and the outermost pixel with an *observed* column density of 1×10^{20} atoms cm^{-2}. Note that $E_{\rm H\,I}$ is conceptually different from the H I radius $R_{\rm H\,I}$ (measured in Chapter 4), as the latter is defined as the radius where the azimuthally-averaged H I surface density

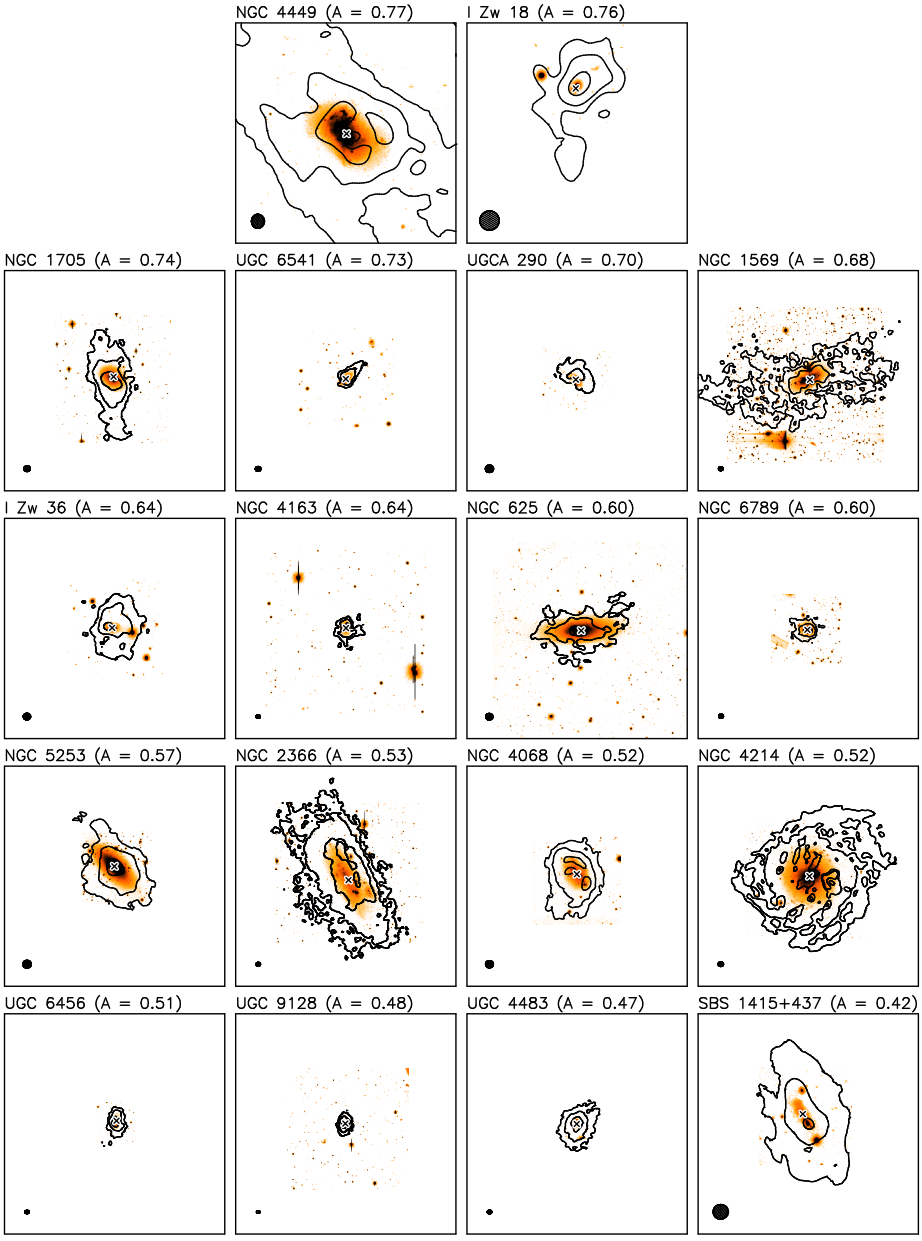

Figure 6.1 – Total H I maps for the 18 starbursting dwarfs in our sample, superimposed on optical images. Each box has a physical size of 20×20 kpc. The contours are at 1, 4, 16×10^{20} atoms cm^{-2}. The cross shows the optical center. The ellipse to the bottom-left shows the H I beam. The galaxies are ordered according to the value of the asymmetry parameter A (see Sect. 6.4 for details).

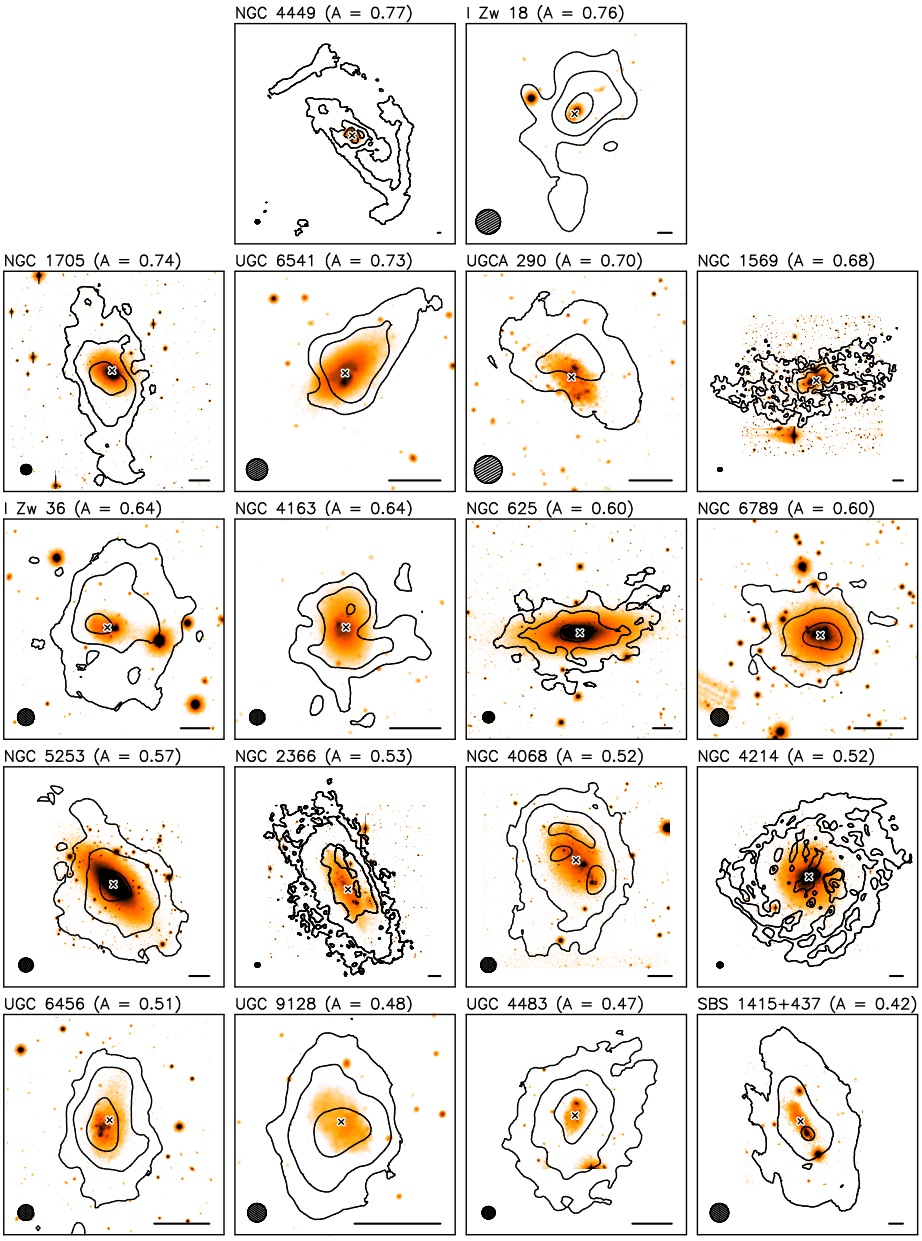

Figure 6.2 – Same as Fig. 6.1, but here the sizes of the boxes have been optimized to show the H I morphology of each galaxy in detail. The bar to the bottom-right corresponds to 1 kpc.

Table 6.4 – Properties of the large-scale H I emission.

Galaxy	$S_{\rm H\,I}$ (Jy km/s)	$M_{\rm H\,I}$ ($10^7 M_\odot$)	$E_{\rm H\,I}$ (amin)	$E_{\rm H\,I}$ (kpc)	$E_{\rm H\,I}/R_{\rm opt}$	$t_{E_{\rm H\,I}}$ (Gyr)	A
NGC 625	27.0	9.7±2.2	4.7	5.4	1.6	1.1	0.60
NGC 1569	106.6	29.1±4.5	10.8	10.7	3.6	1.3	0.68
NGC 1705	18.2	11.1±2.9	4.0	5.9	3.9	0.5	0.74
NGC 2366	254.8	62±17	10.1	9.4	2.1	1.1	0.53
NGC 4068	34.2	14.9±1.6	3.6	4.5	2.5	0.7	0.52
NGC 4163	7.2	1.5±0.2	2.3	2.0	2.0	1.2	0.64
NGC 4214	250.8	43±8	10.4	8.2	3.7	0.6	0.52
NGC 4449$^\alpha$	721.2	300±77	34.3	42	13	7.4	0.77
NGC 5253	47.6	13.8±3.4	4.6	4.7	2.2	...	0.57
NGC 6789	5.9	1.8±0.3	1.8	1.9	2.7	0.2	0.60
UGC 4483	12.0	2.9±0.5	2.7	2.5	4.2	0.8	0.73
UGC 6456	10.4	4.5±0.5	1.9	2.4	1.9	1.5	0.51
UGC 6541	2.8	1.2±0.2	1.9	2.3	2.5	...	0.73
UGC 9128	11.1	1.3±0.2	1.8	1.2	2.0	0.3	0.48
UGCA 290	1.35	1.4±0.2	1.1	2.1	2.3	...	0.70
I Zw 18	2.7	21±4	1.6	8.5	17	1.4	0.76
I Zw 36	8.2	6.7±1.3	1.9	3.3	3.7	0.7	0.64
SBS 1415+437	4.6	20.1±4.6	1.8	7.3	3.0	2.5	0.42

Notes. $^\alpha$the VLA data miss diffuse H I emission (Hunter et al. 1998), thus the values of $S_{\rm H\,I}$ and $M_{\rm H\,I}$ should be considered as lower limits.

profile (corrected for inclination) reaches 1 $M_\odot$ pc^{-2} ($\sim$1.2$\times$10^{20} atoms cm^{-2}). Since $E_{\rm H\,I}$ is *not* obtained from an azimuthal average over the total H I map, it properly takes into account anomalous extensions in the H I distribution (such as tails or filaments), but may be affected by projection effects along the line of sight. Table 6.4 lists the values of $E_{\rm H\,I}$ and $E_{\rm H\,I}/R_{\rm opt}$, where the optical radius $R_{\rm opt}$ is the defined as 3.2 exponential scale-lengths (see Chapter 4) and is given in Table 6.1. For the 18 galaxies in our sample, $E_{\rm H\,I}/R_{\rm opt}$ ranges from $\sim$1.5 to $\sim$4, except for I Zw 18 ($E_{\rm H\,I}/R_{\rm opt} \simeq 17$) and NGC 4449 ($E_{\rm H\,I}/R_{\rm opt} \simeq 13$). These two objects show exceedingly extended H I tails with relatively-high column densities ($\sim 1-2\times10^{20}$ atoms cm^{-2}). Intriguingly, both I Zw 18 and NGC 4449 have a companion galaxy with $L_{\rm R} \simeq 0.5-1\times10^7\ L_\odot$ at a projected distance $\lesssim$ 10 kpc. For I Zw 18, there are strong indications that the extended H I emission is associated with the secondary body (see Lelli et al. 2012a). For NGC 4449, instead, the relation between the companion galaxy and the long H I filaments is unclear (see Martínez-Delgado et al. 2012).

Finally, we describe the kinematics of the large-scale H I emission. Figure 6.3 shows the velocity fields of our 18 galaxies; the size of each box is the same as in Fig. 6.2. As we stressed in Sect. 6.2, these velocity fields are uncertain due to the complex structure of the H I profiles, but they provide an overall

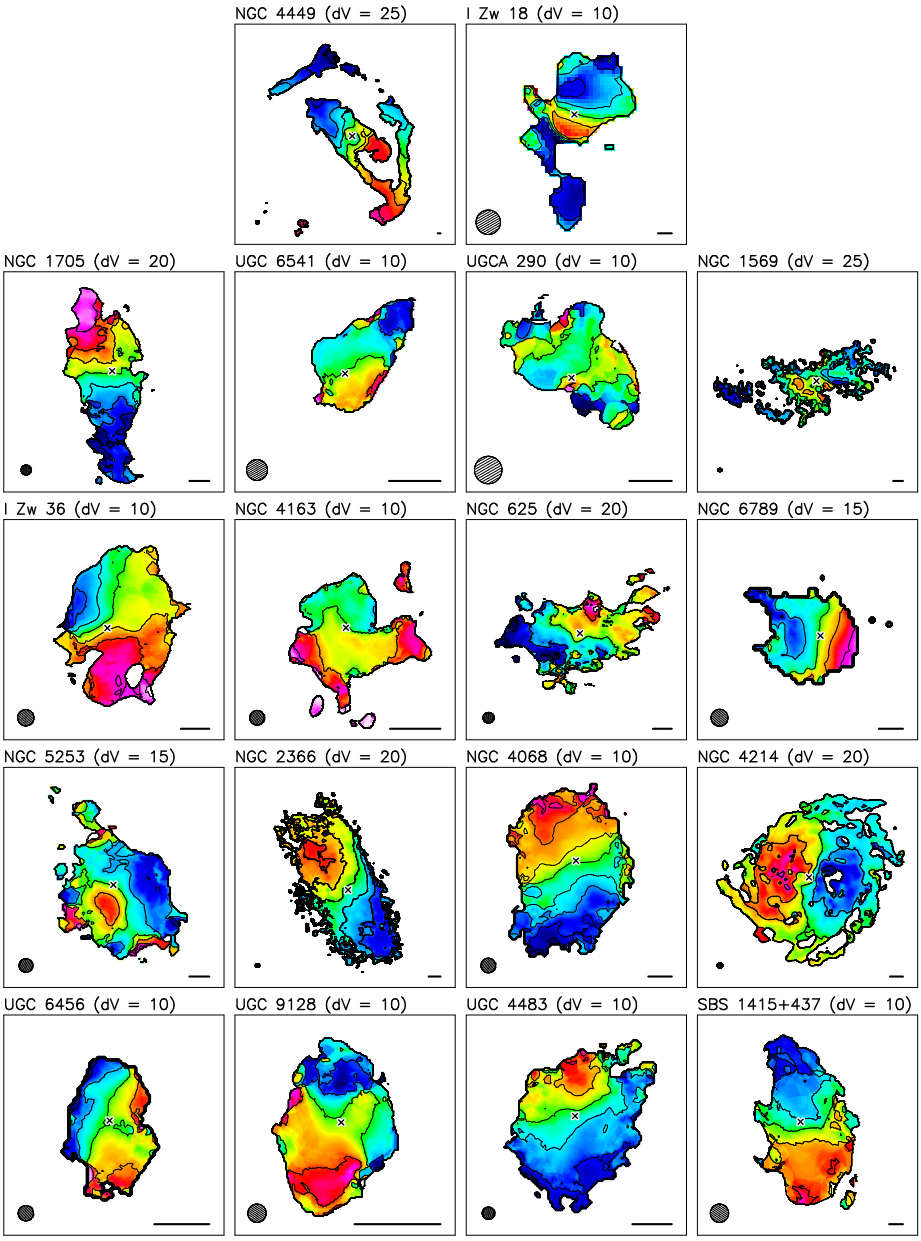

Figure 6.3 – Velocity fields for the 18 starbursting dwarfs in our sample, using the same box-sizes as in Fig. 6.2. The velocity separation dV between the contours is indicated. The cross shows the optical center. The ellipse to the bottom-left shows the H I beam. The bar to the bottom-right corresponds to 1 kpc.

description of the gas kinematics. For BCDs with a rotating H I disk, the outer gas is generally kinematically-connected to the inner H I distribution (except for I Zw 18, discussed in Lelli et al. 2012a). This suggests that the outer tails/extensions may be involved in the overall rotation and could possibly become regularized in a few orbital times. We calculated the orbital times $t_{\mathrm{E_{H\,I}}}$ at $E_{\mathrm{H\,I}}$ using the rotation velocities estimated in Chapter 4 (given in Table 6.1). These rotation velocities are typically estimated at ∼1 to 2 R_{opt}, thus we are extrapolating their values to larger radii by assuming that the rotation curve is flat and the outer gas lies approximately in the same plane as the inner H I disk. The values of $t_{\mathrm{E_{H\,I}}}$ in Table 6.4, therefore, should be considered as order-of-magnitude estimates. Despite these uncertainties, the orbital times at $E_{\mathrm{H\,I}}$ are consistently of the order of ∼0.5 to 1 Gyr (except for NGC 4449 with $t_{\mathrm{E_{H\,I}}} \simeq 7$ Gyr), indicating that the outer asymmetries are relatively-recent and possibly short-lived (see also Sect. 6.4.3).

6.4 Quantifying the H I asymmetry

6.4.1 The asymmetry parameter

To investigate the relation between the large-scale H I emission and the starburst, it is desirable to quantify the degree of asymmetry/lopsidedness in the H I distribution of each individual galaxy. The infrared/optical morphologies of galaxies are usually quantified using the Concentration-Asymmetry-Smoothness (CAS) parameters (Conselice 2003) and the Gini-M_{20} parameters (Lotz et al. 2004). Recently, Holwerda et al. (2011a,b,c,d, 2013) used these parameters to quantify the H I morphologies in several samples of nearby galaxies. In particular, Holwerda et al. (2011c) used total H I maps from the WHISP survey and found that the CAS and Gini parameters weakly correlate with previous *visual* classifications of morphological lopsidedness (by Swaters et al. 2002 and Noordermeer et al. 2005). Particular combinations of the asymmetry parameter $\mathcal{A}$ and the Gini-M_{20} parameters, however, may be able to identify interacting galaxies (Holwerda et al. 2011a,d). Holwerda et al. (2013) used total H I maps at $\sim 5''$ resolution from LITTLE-THINGS (Hunter et al. 2012) and VLA-ANGST (Ott et al. 2012), and argued that the values of the CAS parameters do not strongly depend on the diffuse H I emission on large-scales, observed in total H I maps at lower spatial resolutions (see their Sect. 3.2 and Fig. 2). We consider here the asymmetry parameter $\mathcal{A}$. This is usually defined as

$$\mathcal{A} = \frac{\sum_{i,\,j} |I(i,j) - I_{180^\circ}(i,j)|}{\sum_{i,j} |I(i,j)|} \tag{6.1}$$

where $I(i,j)$ and $I_{180}(i,j)$ are, respectively, the flux densities of a pixel at position (i,j) in the original image and in an image rotated by 180° with respect to the galaxy center. This definition normalizes the residuals between

the original image and the rotated image to the total flux. It is clear, therefore, that asymmetries in the outer parts may have negligible weight in the sum, since the flux densities in the outer regions can be ∼2 orders of magnitude lower than those in the inner regions. Since we want to give more weight to the large-scale asymmetries in the outer parts, we define A as

$$A = \frac{1}{N} \sum_{i,j}^{N} \frac{|I(i,j) - I_{180^\circ}(i,j)|}{|I(i,j) + I_{180^\circ}(i,j)|} \tag{6.2}$$

where N is the total number of pixels in the image. This definiton normalizes the residuals at position (i, j) to the *local* flux density. In particular, if H I emission is detected only on one side of the galaxy, the residuals at (i, j) and $(i, j)_{180^\circ}$ get the maximum value $(= 1)$.

In Figs. 6.1 and 6.2, the total H I maps of our 18 galaxies are ordered according to their value of A. It is clear that A provides a reliable quantification of the H I asymmetry, in close agreement with our visual classification: galaxies with heavily-disturbed and/or strongly offset H I distributions have $A \gtrsim 0.6$, whereas galaxies with minor asymmetries and/or lopsided H I morphologies have $A \lesssim 0.6$. The value of A, however, depends on i) the assumed galaxy center, ii) the column density sensitivity of the H I observations, and iii) the spatial resolution in terms of both the actual beam-size in kpc and the relative number of beams across the H I map. In the following, we describe the effects of these factors on the value of A.

We adopted the optical centers derived in Chapter 4 and listed in Table 6.1. We did not consider the *kinematic* centers because 50% of the galaxies in our sample have either a kinematically-disturbed H I disk or an unsettled H I distribution, thus the kinematic parameters are either very uncertain or undefined (see Chapter 4). Moreover, the use of the optical center correctly returns high values of A for galaxies that show a strong offset between the H I distribution and the stellar body (e.g. NGC 1705 and UGCA 290), that may indicate a recent interaction/accretion event. We checked that small changes in the value of the centers (∼2″) do not significantly affect the value of A (the differences are $\lesssim 0.05$). This is expected because i) the typical uncertainties on the position of the optical center (∼ 1″ to 2″) are much smaller than the H I beam ($\gtrsim 20''$), and ii) high-column-density asymmetries in the inner parts, given our definition of A, do not have much weight.

Regarding the column density sensitivity, the values of A listed in Table 6.4 have been calculated considering only pixels with $N_{\rm H\,I} \geq 10^{20}$ cm^{-2}, since this corresponds to the pseudo-3σ contour of our total H I maps (see Sec. 6.2 and Appendix 6.A). To test the effect of this column density threshold, in Fig. 6.4 (top) we compare the values of A obtained by considering thresholds of 1 and 2×10^{20} cm^{-2}. The differences in A are within ∼0.1 and do not show a systematic trend, implying that the detailed shape of the outermost contour in the total H I map does not strongly affect the value of A. We warn, however,

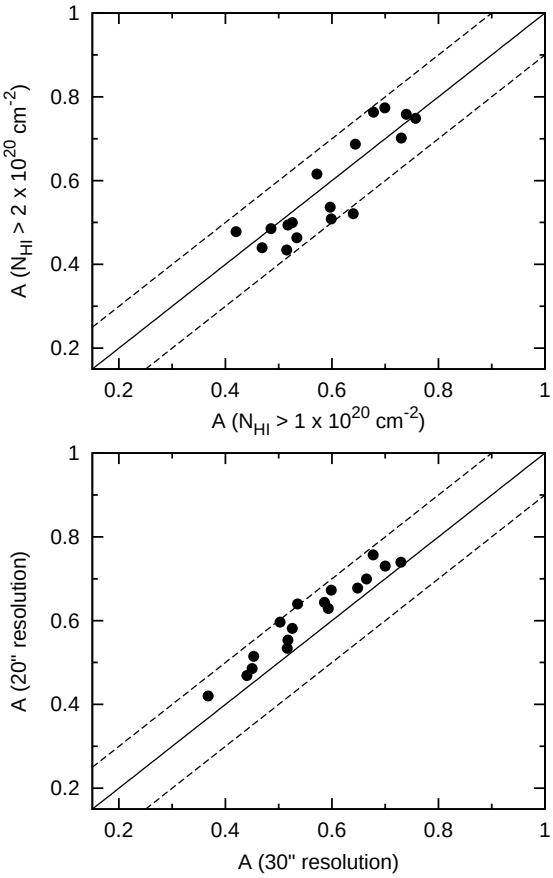

Figure 6.4 – The dependence of the asymmetry parameter A on the $N_{\rm H\,I}$-treshold (*top*) and the spatial resolution of the total H I maps (*bottom*). In the top panel, dots show the values of A obtained from the total H I maps in Figs. 6.1 and 6.2, using a $N_{\rm H\,I}$-treshold of 1 and 2×10^{20} atoms cm^{-2}. In the bottom panel, dots show the values of A using H I maps at $20''$ and $30''$, and a fixed $N_{\rm H\,I}$ of 10^{20} atoms cm^{-2}. The solid line corresponds to a null variation in the value of A, whereas the dashed lines correspond to variations of ± 0.1. See Sect. 6.4.1 for details.

that the use of a column-density threshold provides reliable results as long as i) one does *not* consider values much below the pseudo-3σ contour, introducing noise in the total H I maps, and ii) one does *not* consider high column density thresholds (e.g. $N_{\rm H\,I} \gtrsim 5 - 10 \times 10^{20}$ cm^{-2}), probing the small-scale clumpiness of the H I distribution. We also note that, when using a fixed column-density treshold for different galaxies, the inclination i of the H I disk may introduce some systematic effects, given that *projected* column densities correspond to different *face-on* surface densities. For an optically-thin H I disk, the projected column-density increases with $1/\cos(i)$, thus inclination effects on the column-density threshold become important only in edge-on disks with $i \gtrsim 70°$, for which projected column densities of $\sim 1 \times 10^{20}$ cm^{-2} would correspond to face-on surface densities that are lower by a factor $\gtrsim 3$. In our galaxy sample, the inclinations of the H I disks are $\lesssim 70°$ (see Chapter 4), thus projection effects are not a serious concern here.

The spatial resolution of the H I observations deserves some attention in the derivation of A. To quantify the effects of beam smearing, we constructed total H I maps at 20″ and 30″ resolution for all the galaxies in our sample (except for NGC 4449 that has H I data at a native resolution of ∼60″). The respective values of A, calculated using a threshold of 1×10^{20} cm^{-2}, are compared in Fig. 6.4 (bottom). As expected, total H I maps at higher resolutions systematically yield higher values of A. The differences in A, however, appear reasonably small (within 0.1). Galaxies with a small number of beams along the major axis of the H I disk (e.g. NGC 4163, NGC 6789, I Zw 18) typically show the largest differences in A (∼0.1), whereas galaxies with well-resolved H I maps (e.g. NGC 2366, NGC 1569, and NGC 4214) show very small differences ($\lesssim$0.03). For the latter galaxies, a severe smoothing of the H I data down to 60″ (a factor 3) would still give differences in $A \lesssim 0.1$. Thus, we draw the following conclusions: i) to have a reliable estimate of A, one needs at least ∼5 resolution elements along the major axis of the total H I map, and ii) when the previous condition is met, differences in spatial resolution by a factor of ∼3 give relatively-small differences in A ($\lesssim 0.1$). The total H I maps in Figs. 6.1 and 6.2 are all reasonably well-resolved and have linear resolutions ranging from ∼0.3 to ∼0.7 kpc (see Table 6.3), thus it makes sense to compare the relative values of A. Exceptions are NGC 4449, I Zw 18, and SBS 1415+437, that have total H I maps with linear resolutions $\gtrsim$1 kpc. Despite the low linear resolution, NGC 4449 and I Zw 18 show the highest values of A in our sample, indicating that data at higher resolutions would only increase the difference with the other galaxies. On the contrary, SBS 1415+437 has the lowest value of A in our sample (see Figs. 6.1 and 6.2); this may be an effect of beam-smearing, thus the value of A for SBS 1415+437 may be slightly underestimated with respect to those of other galaxies. We did not build total H I maps at the same linear resolution (in kpc) for all the galaxies because it is not possible to find a compromise between the required number of beams along the H I major axis ($\gtrsim 5$ in order to have a proper estimate of A) and the 3σ column density sensitivity ($\lesssim 1\times10^{20}$ in order to probe the outer, diffuse H I emission).

6.4.2 Comparison with typical irregulars

In this section, we estimate A for a sample of typical Irrs, and make a comparison with our sample of starbursting dwarfs. We use total H I maps from the VLA-ANGST survey (Ott et al. 2012), which provides multi-configuration VLA observations for 29 low-mass galaxies included in the *Advanced Camera for Surveys Nearby Galaxy Survey Treasury* (ANGST; Dalcanton et al. 2009). Similarly to our 18 starbursting dwarfs, these Irrs have been resolved into single stars by HST, and SFHs are available for most of them (Weisz et al. 2011). In order to have two galaxy samples that span a similar range of stellar and H I masses, we excluded objects with $M_{\rm B} \lesssim -11$ (nearly equivalent to $M_* \lesssim 10^7$ M$_\odot$), given that such very low-mass dwarfs are not present in our

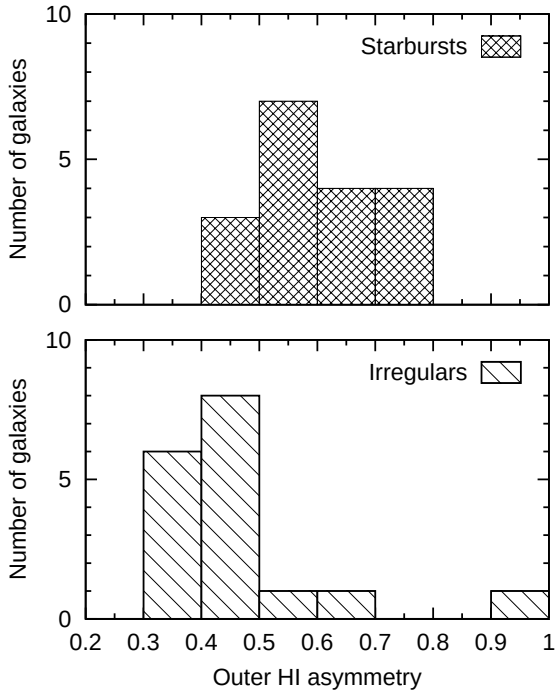

Figure 6.5 – The asymmetry parameter A for our sample of 18 starbursting dwarfs and for a control-sample of 17 typical Irrs, drawn from the VLA-ANGST survey. Starbursting dwarfs clearly have more asymmetric H I morphologies in the outer parts than typical Irrs of similar masses. See Sect. 6.4.2

sample of BCDs. We also excluded AO 0952+69 (Arp's loop), that may be a feature in the spiral arm of M81 (Ott et al. 2012), or a tidal dwarf galaxy (Weisz et al. 2011). The VLA-ANGST sample also contains 3 starbursting dwarfs that are included in our sample (NGC 4163, UGC 4483, and UGC 9128), which we use to test the consistency between our total H I maps and the VLA-ANGST ones. Our final control-sample of typical Irrs, therefore, contains 17 galaxies. Since the SFHs from Weisz et al. (2011) have been obtained by averaging the SFR over a single time-bin in the last ∼1 Gyr, we cannot check whether these galaxies have a recent birthrate parameter $b \lesssim 3$, confirming that they are non-starbursting Irrs. However, as far as we are aware of, these 17 galaxies do not show any sign of recent starburst activity and, thus, we consider them representative for quiescent Irrs.

The natural-weighted H I maps from VLA-ANGST have both an adequate number of resolution elements along the H I major axis, and a 3σ column density sensitivity $\lesssim 10^{20}$ cm^{-2} (see Ott et al. 2012), thus we can safely calculate A using a column-density threshold of 10^{20} cm^{-2} (as for our starbursting dwarfs). The linear resolutions of these H I maps range from ∼60 to ∼200 pc, significantly higher compared to our own H I maps (cf. with Table 6.3). As we discussed in Sect. 6.4.1, this could imply that the values of A for the starbursting dwarfs may be slightly underestimated with respect to those of the VLA-ANGST Irrs.

For UGC 4483 and UGC 9128, however, the VLA-ANGST H I maps and our total H I maps yield remarkably consistent results: UGC 4483 has $A = 0.469$ from our map and $A = 0.464$ from the VLA-ANGST one, while UGC 9128 has $A = 0.485$ from our map and $A = 0.480$ from the VLA-ANGST one. NGC 4163, instead, shows a significant discrepancy: our map yields $A = 0.64$ while the VLA-ANGST one returns $A = 0.50$. The VLA-ANGST map of NGC 4163, indeed, does not trace the full extent of the H I tail to the West and does not detect the cloud complexes to the South (compare our Fig. 6.2 with Fig. 18 of Ott et al. 2012). This is likely due to a different masking of the H I emission for the derivation of the total H I map. We are confident that these H I features are real given that they have been detected also by Swaters et al. (2002) using WSRT data.

Fig. 6.5 compares the values of A for our sample of starbursting dwarfs with those for the VLA-ANGST sample of typical Irrs. Clearly, starbursting dwarfs have systematically higher values of A than typical Irrs: the mean and median values of A are, respectively, 0.60 ± 0.10 and 0.60 for the sample of BCDs, and 0.47 ± 0.16 and 0.41 for the control-sample of Irrs. Moreover, since the total H I maps of the BCDs have lower linear resolutions than those of Irrs, the difference between the two samples may be even larger. Given the possible effects of beam smearing on A, we did not perform a statistical analysis of the two distributions (e.g. using a Kolmogorov-Smirnoff test). It is clear, however, that BCDs generally have more asymmetric H I morphologies in their outer regions than typical Irrs, suggesting that some *external mechanism* triggered the starburst. The two samples have some overlap between $0.4 \lesssim A \lesssim 0.6$ due to the presence of Irrs with lopsided H I morphologies. This is not surprising, as lopsidedness is a common phenomenon among gas-rich galaxies (e.g. Swaters et al. 2002).

Two galaxies from the control-sample have very high values of A, comparable with those of the most disturbed BCDs. These objects are NGC 404 ($A = 0.67$) and DDO 6 ($A = 1$). NGC 404 is at the high-mass end of the dwarf classification ($M_{\rm B} \simeq -16.2$) and shows an unusual lenticular morphology for a dwarf galaxy. Several authors (e.g. Thilker et al. 2010) argued that NGC 404 may have experienced a merger in the last ~1 Gyr, given that it shows a very extended, outer H I ring (del Río et al. 2004); recent, low-level star-formation along the ring (Thilker et al. 2010); a counter-rotating, inner stellar core (Bouchard et al. 2010); and may also host an intermediate mass black hole (Binder et al. 2011). Considering all these facts, the relatively-high value of A may not be surprising, and demonstrates that our definition of A can successfully identify past interacting/merging systems. Regarding DDO 6, both Skillman et al. (2003) and Weisz et al. (2011) classified this object as a "transition" dwarf, i.e. a low-mass galaxy with detected H I emission but little or no Hα flux (Mateo 1998). In DDO 6, H I emission is detected only to the southern part of the galaxy (similarly to UGC 6541 in our sample), hence the galaxy has

an extremely high value of A. It would be interesting to investigate whether this galaxy has experienced a recent starburst. Intriguingly, the well-studied "transition" dwarf Antlia in the Local Group has been classified as a starburst by McQuinn et al. (2012), and shows a H I distribution similar to DDO 6 and UGC 6541 (see Ott et al. 2012; Antlia is not included here because it has $M_{\rm B} \lesssim -11$).

6.4.3 H I asymmetries versus starburst properties

We now investigate the possible relations between A and the properties of the starburst as derived from the HST studies of the resolved stellar populations. We consider the following quantities (see Table 6.2):

1. the birthrate parameter $b = {\rm SFR_p}/\overline{\rm SFR}_{0-6}$, where ${\rm SFR_p}$ is the peak SFR over the past 1 Gyr and $\overline{\rm SFR}$ is the average SFR over the past 6 Gyrs (see McQuinn et al. 2010);

2. the peak SFR surface density $\Sigma_{\rm SFR}(t_{\rm p}) = {\rm SFR_p}/(\pi R^2_{\rm opt})$, where the optical radius $R_{\rm opt}$ is defined as 3.2 exponential scale-lengths (see Chapter 4 and Swaters et al. 2002);

3. the recent SFR surface density $\Sigma_{\rm SFR}(0) = {\rm SFR_0}/(\pi R^2_{\rm opt})$, where ${\rm SFR_0}$ is the average SFR over the last 10 Myr;

4. the specific SFRs (sSFRs) given by ${\rm SFR_0}/M_*$ and ${\rm SFR_p}/M_*$;

5. the look-back time $t_{\rm p}$ at ${\rm SFR_p}$.

In particular, $t_{\rm p}$ allows us to distinguish between "old" bursts (with $t_{\rm p} \gtrsim 100$ Myr) and "young" bursts (with $t_{\rm p} \lesssim 100$ Myr), and can be considered as the typical "age" of the starburst. The SFHs of 5 galaxies (NGC 2366, NGC 4068, UGC 4483, UGC 9128, and SBS 1415+437) show two distinct peaks with similar SFRs (consistent within 1σ). In these cases, we consider the SFR and the look-back time of the older peak, since this is the one that formed more stars, given that the SFR is averaged over a larger time-bin (typically a factor of $\sim$4, see McQuinn et al. 2010). For UGC 6541 and I Zw 36, the recent SFHs are not well constrained (see Schulte-Ladbeck et al. 2000, 2001), thus we have no robust estimate of $\Sigma_{\rm SFR}(t_{\rm p})$, ${\rm sSFR_p}$, and $t_{\rm p}$.

Fig. 6.6 shows that there are no strong trends between A and the SFR indicators $\Sigma_{\rm SFR}(0)$, $\Sigma_{\rm SFR}(t_{\rm p})$, sSFR(0), or sSFR($t_{\rm p}$). We also found no correlation with b. The lack of any real trend has been tested by calculating the Pearson's correlation coefficient $\rho_{\rm cc}$, where $\rho_{\rm cc} = \pm 1$ for an ideal linear correlation/anticorrelation, whereas $\rho_{\rm cc} = 0$ if no correlation is present. We found values of $\rho_{\rm cc} \simeq 0.3$ to 0.4, except for the $A - \Sigma_{\rm SFR}(t_{\rm p})$ diagram that yields $\rho_{\rm cc} \simeq 0.6$. In particular, the 3 galaxies with the highest values of A (NGC 4449, I Zw 18, and NGC 1705) also have the highest values of $\Sigma_{\rm SFR}(t_{\rm p})$ and $\Sigma_{\rm SFR}(0)$.

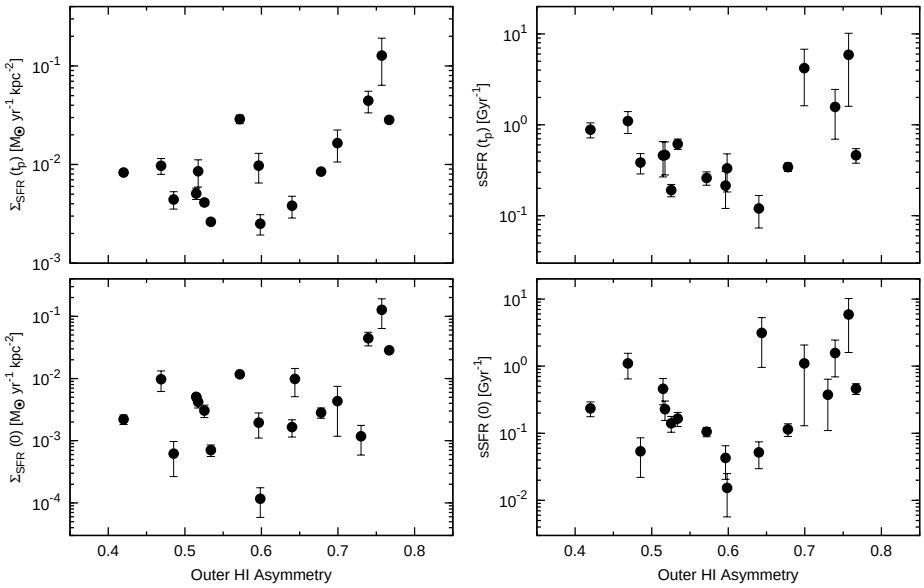

Figure 6.6 – The asymmetry parameter A versus the current SFR surface density $\Sigma_{\rm SFR}(0)$ (*top-left*), the peak SFR surface density $\Sigma_{\rm SFR}(t_{\rm p})$ (*bottom-left*), the current specific SFR (*top-right*), and the peak specific SFR (*bottom-right*). See Sect. 6.4.3 for details.

In these three cases, $t_{\rm p} \simeq 10$ Myr, thus $\Sigma_{\rm SFR}(t_{\rm p}) \simeq \Sigma_{\rm SFR}(0)$. Fig. 6.7 (left) shows that a very clear trend is present between A and $t_{\rm p}$ ($\rho_{\rm cc} \simeq -0.7$): galaxies hosting a "young" burst generally have a more asymmetric H I distribution than galaxies hosting an "old" one, further suggesting a close link between the outer, disturbed gas morphology and the central, recent starburst activity. Galaxies with minor asymmetries ($A \lesssim 0.6$) have values of $t_{\rm p} \simeq 500$ Myr (apart for UGC 6456), which are comparable within a factor of $\sim$2 with the orbital times $t_{\rm E_{H\,I}}$ at the outermost radii $E_{\rm H\,I}$. This is shown in Fig. 6.7 (right), where we plot A against the ratio $t_{\rm p}/t_{\rm E_{H\,I}}$. We recall, however, that $t_{\rm E_{H\,I}}$ is an order-of-magnitude estimate, thus the ratio $t_{\rm p}/t_{\rm E_{H\,I}}$ provides only a rough measure of the number of orbits that the outer gas may have completed since the epoch of the strongest star-formation activity. Despite these uncertainties, Fig. 6.7 (right) clearly indicates that galaxies hosting an "old" burst may have had enough time to complete an entire revolution around their center and, therefore, to regularize their outer H I distribution.

Finally, we discuss in some detail the "outlier" UGC 6456 (VII Zw 403) indicated in Fig. 6.7. This galaxy has been recently studied by Simpson et al. (2011), who pointed out the relatively-regular H I morphology and the lack of a clear external trigger. The total H I map and velocity field of Hunter et al. (2012), however, show a tail/extension to the South-West. We also detected this

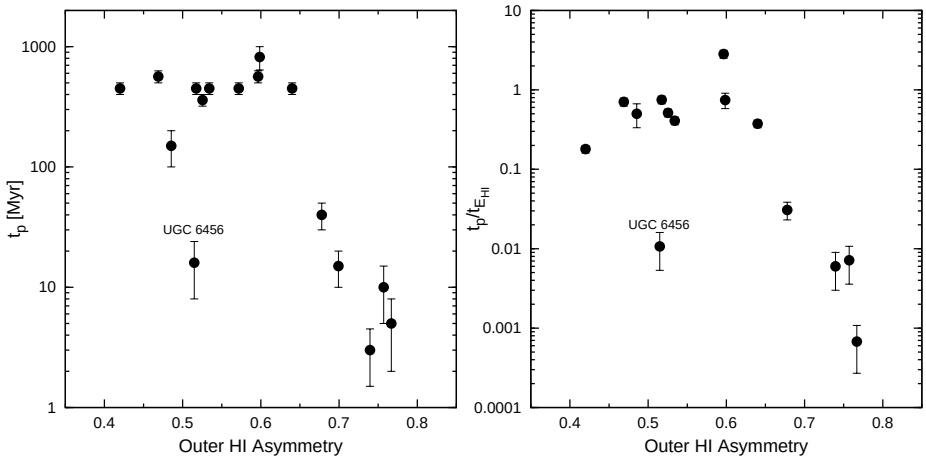

Figure 6.7 – The asymmetry parameter A versus the look-back time $t_{\rm p}$ at the peak of the SFH (*left*) and the ratio $t_{\rm p}/t_{\rm E_{H\,I}}$. See Sect. 6.4.3 for details.

feature in our total H I map, but it is below the 3σ column density sensitivity of the observations, having $N_{\rm H\,I} \lesssim 5 \times 10^{19}$ cm^{-2}. Deeper H I observations are needed to confirm whether this H I tail is real or an observational artefact. The location of UGC 6456 in Figs. 6.6 and 6.7 would change if one adopts column-density thresholds $\lesssim 5 \times 10^{19}$ cm^{-2}, but unfortunately these low values cannot be consistently adopted here due to the limited sensitivity of the H I observations for several galaxies in our sample.

6.5 Individual galaxies and their environment

In the following, we discuss in detail the H I properties of individual galaxies, and describe their nearby environment. We used the NASA/IPAC Extragalactic Database (NED[1]) to search for nearby galaxies with measured redshifts in a velocity range of ± 300 km s^{-1} with respect to the systemic velocity of the starbursting dwarf. Table 6.5 provides the 3 nearest galaxies to each BCD in our sample, together with their basic properties (from Karachentsev et al. 2013). We checked that these objects are actual galaxies by visual inspection, and excluded background/foreground galaxies when accurate, redshift-independent distances were available. Since most of the BCDs considered here have distances $D \lesssim$ 7 Mpc, Table 6.5 should be nearly complete down to dwarf galaxies with total magnitudes $M_{\rm B} \simeq -11$ and mean surface brightnesses $\mu_{\rm B} \simeq 25$ mag arcsec^{-2} (cf. with Karachentsev et al. 2004, 2013). Any galaxy with $M_{\rm B} \gtrsim -10$ would

[1]The NASA/IPAC Extragalactic Database (NED) is operated by the Jet Propulsion Laboratory, California Institute of Technology, under contract with the National Aeronautics and Space Administration.

be more than 10 times less massive than the BCDs in our sample, which have $M_{\rm R} \lesssim -14$ ($M_{\rm B} \lesssim -13$), thus it would probably be unable to induce the strong burst of star-formation. UGC 4483 and UGC 9128 have somewhat fainter luminosities ($M_{\rm R} \simeq -13$) but they are very nearby ($D \lesssim 3$ Mpc), thus possible companions with total magnitudes as low as $M_{\rm B} \simeq -10$ should be catalogued. SBS 1415+437 and I Zw 18, instead, are at distances of ∼14 Mpc and ∼18 Mpc, respectively, thus they may have faint companions that have not been identified by optical surveys. Note that an object with a proper velocity of ∼200 km s^{-1} (out of the Hubble flow) covers ∼200 kpc in 1 Gyr, thus one cannot exclude the possibility that a galaxy at a projected distance $D_{\rm p} \lesssim 200$ kpc from a BCD might have triggered the staburst by a past collision on an hyperbolic orbit (see e.g. Noguchi 1988). Most of the BCDs in our sample have such a potential perturber, except for NGC 1705, NGC 6789, and UGC 9128. Note that typical Irrs often have companions at $D_{\rm p} \lesssim 200$ kpc, thus one cannot claim that the presence of a companion is a *sufficient* condition for a starburst to occur.

Table 6.5 – Environment of the starbursting dwarfs in our sample. The projected distance $D_{\rm p}$ from the nearest galaxies and the difference between their respective systemic velocities $\Delta V_{\rm sys}$ were calculated using NED. The properties of the nearest galaxies are taken from Karachentsev et al. (2013), and given only when their distances are accurately estimated from the TRGB (the distance of NGC 2403 is estimated from Cepheids). Note that objects without an accurate distance estimate may be background/foreground galaxies. The properties of I Zw 18 C are taken from Lelli et al. (2012a). The morphological types are taken from both NED and Karachentsev et al. (2013).

Galaxy	Membership	Nearest galaxies	$D_{\rm p}$ (kpc)	$\Delta V_{\rm sys}$ (km s^{-1})	Type	Dist (Mpc)	$M_{\rm B}$ (mag)	log($M_{\rm H\,I}$) (10^7)	$W_{50,\,\rm H\,I}$ (km s^{-1})
NGC 625	Sculptor group	ESO245-005	203	−7	Im	4.4	-15.6	8.58	60
	(periphery)	CFC97 Sc 24$^{\alpha}$	402	-236	...	...	...	...	92
		GSD 106	619	132	...	...	...	...	...
NGC 1569	IC 432 group	UGCA 92	74	19	Irr	3.0	-15.6	8.17	56
		Cam B	190	157	Irr	3.3	-11.9	7.08	21
		UGCA 86	231	147	Im?	3.0	-17.9	...	...
NGC 1705	Field	LSBG F157-089$^{\beta}$	518	175	...	...	...	...	...
		MRSS 157-121650$^{\gamma}$	562	-50	...	...	...	...	...
		SGC 0409.0-5638	631	242	Irr	...	...	...	...
NGC 2366	M81 group	NGC 2363$^{\delta}$	2	-33	Irr	...	...	...	...
	(periphery)	NGC 2403	206	30	Scd	3.2	-19.2	9.26	240
		Holmberg II	254	39	Im	3.4	-16.7	8.61	64
NGC 4068	CVn I cloud	MCG +09-20-131	135	-47	Irr	4.6	-13.1	7.37	27
		ASK 185765.0$^{\epsilon}$	143	291	...	...	...	...	...
		UGC 7298	145	-33	Irr	4.2	-12.3	7.28	21
NGC 4163	CVn I cloud	MCG +06-27-017$^{\zeta}$	27	181	Im	4.8	-13.0	...	...
		NGC 4190	29	70	Im/BCD	2.8	-13.9	7.46	49
		DDO 113	30	126	Sph?	2.9	-11.5	< 5.56	32
NGC 4214	CVn I cloud	DDO 113	8	-7	Sph?	2.9	-11.5	< 5.56	...
		NGC 4190	23	-63	Im/BCD	2.8	-13.9	7.46	49
		NGC 4163	34	-133	BCD	3.0	-13.8	7.16	32
NGC 4449	CVn I cloud	DDO 125	44	-15	Im	2.7	-14.3	7.48	27
		MCG +07-26-012	77	226	Im	...	...	...	...
		DDO 120	155	252	Im	...	...	...	...

Table 6.5 – continued.

Galaxy	Membership	Nearest galaxies	$D_{\rm p}$ (kpc)	$\Delta V_{\rm sys}$ (km s^{-1})	Type	Dist (Mpc)	$M_{\rm B}$ (mag)	log($M_{\rm H\,I}$) (10^7)	$W_{50,\,\rm H\,I}$ km s^{-1}
NGC 5253	M83 group	ESO444-084$^{\eta}$	54	116	Sc	...	...	...	...
		NGC 5264	108	68	Im	4.5	-15.9	7.65	35
		HIDEEP J1337-33	111	181	Irr	4.4	-11.1	6.67	20
NGC 6789	Local Void	ABELL 2312:[MPC97] 04$^{\theta}$	297	59	...	...	...	...	...
		UGC 11411	400	220	BCD	...	...	...	...
		LEDA 166193	578	290	Irr	...	...	...	28
UGC 4483	M81 group	M81 Dwarf A	92	-45	Irr	3.5	-11.5	7.06	21
		Holmberg II	100	-16	Im	3.4	-16.7	8.61	64
		DDO 53	201	-138	Irr	3.6	-13.4	7.62	30
UGC 6456	M81 group	CGCG 351-049$^{\iota}$	151	8	...	...	...	...	...
	(periphery)	UGC 8245$^{\iota}$	358	172	Im	...	...	...	...
		DDO 82	683	158	Im	4.0	-14.7	...	...
UGC 6541	CVn I cloud	ASK 184683.0	213	208	...	...	...	...	...
	(periphery)	ASK 185765.0$^{\epsilon}$	289	247	...	...	...	...	...
		NGC 3741	292	-21	Im/BCD	3.0	-13.1	7.88	83
UGC 9128	Field	LSBG F650-01$^{\kappa}$	353	-167	...	...	...	...	...
		MAPS O-383-0548118$^{\lambda}$	359	-93	...	...	...	...	...
		SDSS J145657.7+221315$^{\lambda}$	365	-102	...	...	...	...	...
UGCA 290	NGC 4631 group?	UGC 7719	83	210	Sdm	...	...	...	57
		IC 3687	115	114	Im	4.6	-14.6	7.90	36
		BTS 142	122	251	Irr	...	...	...	23
I Zw 18	Field	I Zw 18 C	2	-16	Irr	18.2	-12.1	$\lesssim$ 8.08	$\sim$45
		ASK 153750.0	639	243	...	...	...	...	...
		MGC +09-16-029	1052	-159	...	...	...	...	...
I Zw 36	CVn I cloud	UGC 7639$^{\mu}$	117	105	Im	...	...	...	...
		NGC 4248$^{\nu}$	183	207	...	...	...	...	...
		MAPS O-171-0165792	214	195	...	...	...	...	...

Table 6.5 – continued.

Galaxy	Membership	Nearest galaxies	$D_{\rm p}$ (kpc)	$\Delta V_{\rm sys}$ (km s^{-1})	Type	Dist (Mpc)	$M_{\rm B}$ (mag)	log($M_{\rm H\,I}$) (10^7)	$W_{50,\,\rm H\,I}$ km s^{-1}
SBS 1415+437	Field	MAPS O-221-0093662	179	105	...	...	...	...	...
		ASK 310753.0	492	18	...	...	...	...	...
		NGC 5608	493	47	Im	...	...	...	...

Notes. $^{(\alpha)}$ According to Karachentsev et al. (2004), this galaxy is not in the Sculptor group but lie outside the Local Volume. The value of $W_{50,\,\rm H\,I}$ is taken from Cote et al. (1997).
$^{(\beta)}$ This galaxy may be in the Dorado group ($D \simeq 17$ Mpc, Firth et al. 2006).
$^{(\gamma)}$ This object may be an ultra-compact dwarf in the Dorado group ($D \simeq 17$ Mpc, Evstigneeva et al. 2007).
$^{(\delta)}$ It is unclear whether this object is part of NGC 2366 or a separate galaxy (see Fig. 6.8).
$^{(\epsilon)}$ Trentham et al. (2001) included this galaxy in their study of the Ursa Major cluster. However, ASK 185765.0 is probably not a cluster member, given that its systemic velocity is $\sim$497 km s^{-1} (from the Sloan Digital Sky Survey).
$^{(\zeta)}$ Despite this galaxy is close to NGC 4163 on the sky, it seems to inhabit a more distant part of the CnV I cloud, having a distance of $\sim$4.8 Mpc from the TRGB.
$^{(\eta)}$ This edge-on spiral is not a member of the M83 group and probably is a background galaxy.
$^{(\theta)}$ This object is classified as a galaxy by NED. It is projected on the sky near the galaxy cluster ABELL 2312 (Maurogordato et al. 1997), but its systemic velocity indicates that it is a nearby object. In our opinion, it is unclear whether this is a galaxy or a Galactic object.
$^{(\iota)}$ This object is not associated to the M81 group and may be a background/foreground galaxy.
$^{(\kappa)}$ According to NED, this object may be a planetary nebula.
$^{(\lambda)}$ This object has also been classified as a X-ray source and a star.
$^{(\mu)}$ This object may have $D \simeq 7.1$ Mpc (from surface brightness fluctuations, Karachentsev et al. 2013) and be outside the CVn I cloud.
$^{(\nu)}$ This object may have $D \simeq 7.4$ Mpc (from the Tully-Fisher relation, Karachentsev et al. 2013) and be outside the CVn I cloud.

NGC 625 has a ∼2 kpc H I tail to the North-West, that shows a coherent kinematic structure at $V_{\rm los} \simeq 420$ km s^{-1}. A second tail/extension is present to the South-East, but it does not show a clear kinematic structure. Our total H I map and velocity field are in close agreement with those from Côté et al. (2000) and Cannon et al. (2004). NGC 625 is associated with the core of the Sculptor filament, but it is quite far from the central, massive galaxy NGC 253, being at a projected distance of ∼1.3 Mpc (Karachentsev 2005).

NGC 1569 has a heavily disturbed H I distribution. A H I cloud with $M_{\rm H\,I} \simeq 2 \times 10^7$ M$_\odot$ lies at $V_{\rm los} \simeq -150$ km s^{-1} to the East of the galaxy, and is connected to the main H I distribution by a thin bridge (see also Stil & Israel 1998). The datacube is strongly affected by Galactic emission, thus the total H I map and the velocity field are uncertain. Our results, however, are in close agreement with those from Stil & Israel (1998, 2002) and Johnson et al. (2012). NGC 1569 is part of the IC 432 group of galaxies (Grocholski et al. 2008) and has a nearby companion (UGCA 92) at a projected distance of ∼70 kpc with a similar systemic velocity (within ∼20 km s^{-1}).

NGC 1705 has an extended, warped H I disk. The H I disk has a relatively-regular morphology and kinematics, but it is strongly offset with respect to the stellar component: the optical and kinematic centers differ by ∼550 pc, while the optical and kinematic PAs differ by ∼45° (see Chapter 4). To the North-East, there is also a small H I extension with peculiar kinematics, that may be associated with the Hα wind (see Meurer et al. 1998; Elson et al. 2013). NGC 1705 appears very isolated: the two nearest objects (LSBG F157-089 and MRSS 157-121650) are at a projected distance of ∼0.5 Mpc, but may be members of the Dorado group at $D \simeq 18$ Mpc (see Firth et al. 2006 and Evstigneeva et al. 2007, respectively). Three other objects (NGC 1533, IC 2038, and IC 2039) lie at ∼7° from NGC 1705, but they seem to be background galaxies at distances of ∼20 Mpc (based on the TF relation).

NGC 2366 has a H I disk with a broad extension to the South-East and a strong kinematic distortion to the North-West. Fig. 6.8 (left) shows an optical image overlaid with the H I emission at 15″ resolution, integrated in a narrow spectral range near the systemic velocity (between ∼90 and ∼115 km s^{-1}). The gas to the North-West does not follow the rotation of the H I disk (see also Fig. 3 of Oh et al. 2008) and may be associated with the secondary star-forming body to the South-West (NGC 2363). Fig 6.8 (right) shows a Position-Velocity diagram taken along the dashed-line in Fig. 6.8 (left). Intriguingly, the PV-diagram displays a steep velocity gradient that coincides with the spatial position and optical systemic velocity of NGC 2363 (indicated by the star). However, given the overall rotation of the H I disk of NGC 2366, it is unclear whether this velocity gradient is due to rotation in a local potential well. The NGC 2363/NGC 2366 system probably is an on-going minor merger.

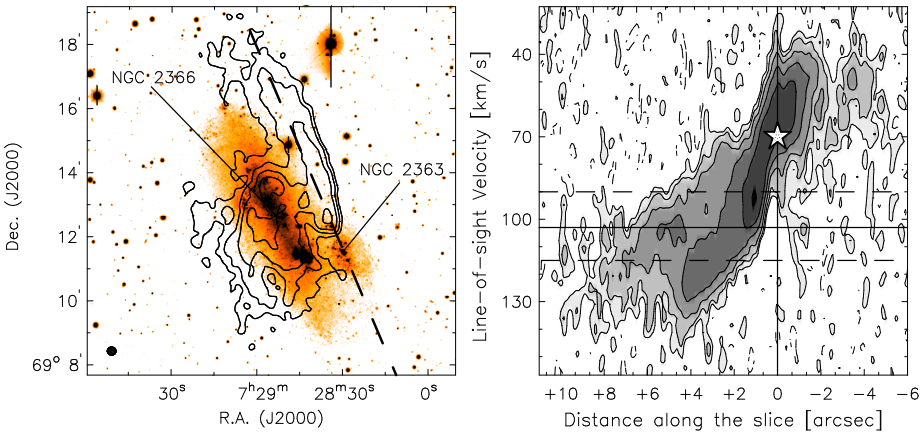

Figure 6.8 – Kinematically-anomalous gas in NGC 2363/NGC 2366. *Left*: V-band image overlaid with the H I emission at 15″ resolution, integrated in a narrow spectral range near the systemic velocity of NGC 2366 (from ∼90 to ∼115 km s^{-1}). The H I column densities are 2, 4, 8, 16 $M_\odot$ pc^{-2}. The arrows indicate the centers of NGC 2363 and NGC 2366. The circle to the bottom-left shows the H I beam. *Right*: Position-Velocity diagram taken along the dashed-line shown in the left-panel. The solid, horizontal line indicates the systemic velocity of NGC 2366 (103 km s^{-1}), while the dashed, horizontal lines show the velocity range that has been used to create the H I map in the left-panel. The vertical line corresponds to the spatial position of NGC 2363, while the star shows its optical systemic velocity (70 km s^{-1}), as given by NED. Contours are at -1.5 (dashed), 1.5, 3, 6, and 12 σ, where $\sigma = 0.66$ mJy/beam.

NGC 4068 shows a broad H I extension to the South-East. This object is in the Canes Venatici I (CVn I) cloud, which is an extended, loose group mainly inhabited by low-mass galaxies (Karachentsev et al. 2003).

NGC 4163 shows a H I tail to the West and, possibly, a second tail to the South (see also Hunter et al. 2012). NGC 4163 is in the CVn I cloud and is close to several other Irrs (at $D_{\rm p} \simeq$30 kpc), including the starbursting dwarf NGC 4214 and the "compact" irregular NGC 4190 (UGC 7232, see Chapter 5). Intriguingly, NGC 4190 has been classified as a BCD by Karachentsev et al. (2013) and shows a disturbed H I morphology (see Swaters et al. 2002).

NGC 4214 has a H I disk with a well-defined spiral pattern. The H I disk is strongly warped (see Chapter 4) and slightly more extended to the North-West. NGC 4214 is in the CVn I cloud and has a small companion galaxy (DDO 113) at a projected distance of ∼8 kpc. DDO 113 likely is a gas-poor spheroidal (Kaisin & Karachentsev 2008). This object, indeed, is within the field-of-view of the VLA, but no H I emission is detected.

NGC 4449 has an exceedingly extended H I distribution characterized by long filaments with column densities of ∼1 M$_\odot$ pc^{-2} (Hunter et al. 1998). A tidally-disturbed stellar body is present to the South-East of the galaxy, but it does not spatially coincide with any gaseous feature (Martínez-Delgado

et al. 2012), thus its relation with the extended H I emission remains unclear. NGC 4449 is one of the most massive galaxies in the CVn I cloud (Karachentsev 2005).

NGC 5253 has a ∼4 kpc H I tail to the North at $V_{\rm los} \simeq 400$ km s^{-1}. Our total H I map at $40'' \times 40''$ resolution is slightly different from that of López-Sánchez et al. (2012) at $57.8 \times 37.5''$ resolution, because we used a Gaussian-smoothed, robust-weighted datacube instead of a natural-weighted datacube. The former cube has a much more regular noise structure than the latter one, providing a better estimate of the 3σ colum density sensitivity. NGC 5253 is in the CenA/M83 group, and its projected distance from the massive spiral galaxy M83 is ∼150 kpc (Karachentsev 2005).

NGC 6789 has a regularly-rotating H I disk with several asymmetric features in the outer parts. This galaxy is in the Local Void and its nearest massive companion (NGC 6946) is at a projected distance of ∼2.5 Mpc (Drozdovsky et al. 2001).

UGC 4483 has a regularly-rotating H I disk with a small extension to the North-West. This galaxy is in the M81 group and lies between the group center and the NGC 2403 sub-group (Karachentsev et al. 2002).

UGC 6456 has a H I disk that is slightly more extended to the South. The datacube is affected by Galactic emission, making the total H I map uncertain. Our results, however, are in close agreement with those from Simpson et al. (2011). UGC 6456 lies in the periphery of the M 81 group (Karachentsev 2005).

UGC 6541 has a very asymmetric H I distribution. Gas emission is detected only in the Northern half of the galaxy. UGC 6541 is located to the North-Western edge of the the CVn I cloud (Karachentsev et al. 2003). Another BCD (NGC 3741, Karachentsev et al. 2013) lies at a projected distance of ∼300 kpc.

UGC 9128 has a relatively-regular H I distribution. The optical and kinematic position angles, however, differ by ∼30° (see also Chapter 4). This galaxy appears very isolated; the closest massive galaxy is the Milky Way at $D \simeq 2.2$ Mpc (Karachentsev et al. 2013).

UGCA 290 has a peculiar H I distribution that is off-set with respect to the stellar component. Our total H I map at $20'' \times 20''$ resolution is less extended than the one obtained by Kovač et al. (2009) using WSRT data at $52.2'' \times 30.9''$ resolution, but the H I fluxes are consistent within the uncertainties, indicating that our total H I map is not missing diffuse H I emission. UGCA 290 may be part of the NGC 4631 group; its projected distance from NGC 4631 is ∼700 kpc.

I Zw 18 has been discussed in details by Lelli et al. (2012a). The total H I map presented here is slightly different from that in Lelli et al. (2012a) because it was constructed using a mask at $60''$ resolution (instead of $45''$ resolution) for consistency with the other galaxies. The most likely interpretation of this system is an interaction/merger between two (or more) gas-rich dwarfs.

I Zw 36 has an extended and asymmetric H I distribution, that is kinematically-connected to a central rotating disk (see Chapter 4 and Ashley

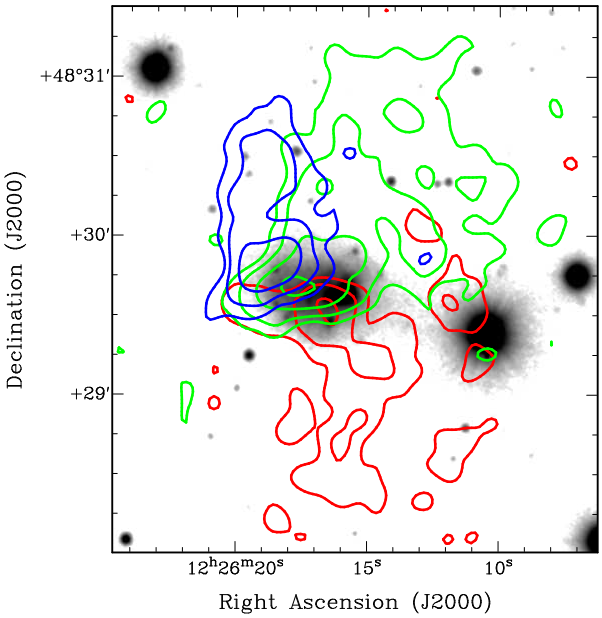

Figure 6.9 – Large-scale H I emission in I Zw 36 at 10″ resolution, integrated across 3 velocity ranges: 250 to 260 km s^{-1} (blue), 275 to 285 km s^{-1} (green), and 300 to 310 km s^{-1} (red). Contours are at 1.2, 2.4, 4.8, and 9.6 M$_\odot$ pc^{-2}.

et al. 2013). Data at 10″ resolution (see Fig. 6.9) reveal that the H I emission forms a tail-like structure to the South at receding velocities ($V_{\rm los} \simeq 300$ to 310 km s^{-1}; $V_{\rm sys} = 277$ km s^{-1}) and a broad extension to the North near the systemic velocity ($V_{\rm los} \simeq 270$ to 290 km s^{-1}), possibly connected to the approaching side of the disk ($V_{\rm los} \simeq 250$ to 260 km s^{-1}). There are no optical features associated with the extended gas down to $\mu_{\rm R} \simeq 26$ mag arcsec^{-2}. I Zw 36 is in the CVn I cloud.

SBS 1415+437 has an extended, lopsided H I disk. The galaxy is at a relatively-large distance (∼13.6 Mpc), thus it is possible that faint, nearby companions have not been identified by optical surveys.

6.6 Discussion

In Sect. 6.3, we found that starbursting dwarfs show a broad, continuous range of H I morphologies. Several BCDs in our sample have heavily disturbed H I morphologies, characterized by strong asymmetries, long filaments, and/or severe offsets between the stellar and H I distributions. Other galaxies, instead, show minor asymmetries, characterized by H I extensions and/or small tails in the outer parts. In Sect. 6.4, we introduced the parameter A, that quantifies the large-scale asymmetry in the outer parts, and measured it for both our sample of BCDs and a control-sample of typical Irrs. We found that starbursting dwarfs systematically have more asymmetric H I morphologies that typical Irrs,

suggesting that the starbursts have been triggered by some *external mechanism*. There is, however, a "grey area" for $0.4 \lesssim A \lesssim 0.6$, where one can find both starbursting and non-starbursting dwarfs with lopsided H I morphologies. Lopsidedness is a common phenomenon among spirals and irregular galaxies (e.g. Baldwin et al. 1980; Verheijen & Sancisi 2001; Swaters et al. 2002), and it has been suggested that it may be due to relatively-old interactions and/or accretion events (e.g. Sancisi et al. 2008). Our results are in line with this hypothesis, as we now discuss.

In Sect. 6.4, we also compared A with the starburst properties, as derived from the HST studies of the resolved stellar populations. We found that the H I asymmetry does not clearly correlate with any starburst indicator (the birthrate parameter, the specific SFR, or the SFR surface density), but there is a significant correlation between A and the look-back time at the peak of the star-formation activity $t_{\rm p}$ (see Fig. 6.7, left). Galaxies hosting an "old" burst ($\gtrsim$100 Myr) have low values of A, while galaxies hosting a "young" burst ($\lesssim$100 Myr) have a progressively more asymmetric H I distribution. This points to a close link between the outer, large-scale H I asymmetries and the central, recent starburst. In particular, galaxies with lopsided H I morphologies ($A \lesssim 0.6$) have values of $t_{\rm p} \simeq 500$ Myr, which are comparable with the orbital times in the outer regions (see Fig. 6.7, right), suggesting that the overall galaxy rotation could have had enough time to regularize the outer H I distribution since the epoch of the interaction/accretion event that possibly triggered the starburst. In particular, BCDs with extended, strongly-warped, and regularly-rotating H I disks, such as NGC 4214 (Chapter 4) and NGC 2915 (Elson et al. 2010), may represent an advanced stage of the interaction/accretion phenomenon, as it has already been suggested by Sancisi et al. (2008). On the other hand, a galaxy like NGC 1705, which has a warped H I disk that is strongly off-set with respect to the stellar component (see Chapter 4), may be in an earlier stage, where the outer H I gas is still in the process of settling down. This is in agreement with the very recent starburst activity ($t_{\rm p} \simeq 3$ Myr) observed in this galaxy (Annibali et al. 2003).

One may argue that the outer H I asymmetries could be the result of gaseous outflows due to stellar feedback. This possibility is very unlikely for the following reasons: i) gaseous outflows are expected to develop along the axis of rotation and to show some bipolar symmetry (e.g. Mac Low & Ferrara 1999), whereas the H I asymmetries discussed here often have a tail-like morphology and do not show any preferential direction with respect to the central galaxy (see Figs. 6.1 and 6.2); ii) the asymmetry parameter A shows no clear trend with the SFR surface density nor with the specific SFR (see Sect. 6.4.3); and iii) the energetics of the stellar feedback suggests that dwarf galaxies with circular velocities $\gtrsim$20 km s^{-1} do not expell a large quantity of gas out of their potential well, unless one assumes a very high feedback efficiency (see Chapter 4 and Ferrara & Tolstoy 2000). We conclude, therefore, that the large-scale H I asymmetries

Table 6.6 – Other starbursting dwarfs with high-quality H I observations.

Name(s)	Properties	References
II Zw 33 (Mrk 1039)	LSB companion II Zw 33 B	Walter et al. (1997)
HS 0822+3542	LSB companion SAO 0822+3542	Chengalur et al. (2006)
Mrk 324 (UGCA 439)	LSB companion EXG 0123-0040; H I tail?	van Zee et al. (2001)
NGC 2537 (Mrk 86)	Companion IC 2233 (Sd); outer H I arm	Matthews & Uson (2008)
UM 461/UM 462	BCD pair with lopsided H I disks	van Zee et al. (1998)
Haro 4 (Mrk 26)	Possible interaction with NGC 3510 (Sm)	Bravo-Alfaro et al. (2004)
Mrk 108 (IC 2450)	Interacting with NGC 2814 (Sb) & NGC 2820 (Sc)	Kantharia et al. (2005)
II Zw 70/ II Zw 71	Interacting pair	Cox et al. (2001)
SBS 0335-052	Interacting pair	Pustilnik et al. (2001a); Ekta et al. (2009)
SBS 1129+576/577	Interacting pair	Ekta et al. (2006)
II Zw 40 (UGC 116)	Advanced merger	van Zee et al. (1998)
IC 10 (UGC 192)	Long H I filaments and plumes	Manthey & Oosterloo (2008)
Haro 36 (UGC 7950)	H I filament	Ashley et al. (2013)
Mrk 1418 (UGC 5151)	H I plumes and clouds	van Zee et al. (2001)
FCC 35	High-velocity H I complex	Putman et al. (1998)
Haro 2 (Mrk 33)	H I extension and small tail/cloud	Thuan et al. (2004)
NGC 4861 (UGC 8098)	H I disk extended towards a H I cloud	Thuan et al. (2004)
Mrk 900 (NGC 7077)	Lopsided H I disk	van Zee et al. (2001)
Mrk 750	Lopsided H I disk	van Zee et al. (2001)
UM 439 (UGC 6578)	Lopsided H I disk	van Zee et al. (2001)
UM 323	Lopsided H I disk, possibly warped	van Zee et al. (2001)
UM 38	Relatively-regular H I disk	van Zee et al. (2001)
NGC 2915	Extended, warped H I disk	Meurer et al. (1996); Elson et al. (2010)

in the outer regions of BCDs indicate that the starburst is triggered by *external mechanisms*, such as interactions/mergers between gas-rich dwarfs or cold gas accretion from the IGM.

Recent H I studies by Ekta et al. (2008), Ekta & Chengalur (2010), and López-Sánchez et al. (2010) have also highlighted the importance of interaction/accretion events in triggering the starburst in BCDs. In Table 6.6, we list further examples of starbursting dwarfs with high-quality H I observations. This list is by no means complete. We have, however, carefully inspected the published total H I maps and velocity fields of these galaxies, and reported their main properties. These galaxies do *not* have accurate SFHs from HST observations, but are thought to be experiencing a starburst as suggested by their blue colors, high surface brightnesses, and/or strong emission lines. We also have no direct information on the "age" of the starburst. Based on their H I morphology and on the observed trend between A and $t_{\rm p}$, however, we suggest that we may be observing BCDs at different stages of the interaction/accretion process. In particular, we distinguish between four main "classes" or "evolutionary stages":

1. BCDs that have a nearby companion ($\lesssim$ 200 kpc) but show *no* sign of strong interactions, such as H I bridges or tails (e.g. II Zw 33, Walter et al. 1997). These systems may represent either an early-stage prior to a merger or a very-late stage after a fly-by.

2. BCDs that are clearly interacting with a companion (e.g. II Zw 70/II Zw 71, Cox et al. 2001) or are in an advanced stage of merging (e.g. II Zw 40, van Zee et al. 1998).

3. BCDs that are relatively isolated and show a heavily-disturbed H I morphology (e.g. IC 10, Manthey & Oosterloo 2008), that may be due to a recent interaction/merger and/or cold gas accretion from the environment.

4. BCDs that are relatively isolated and have an extended, lopsided H I disk (e.g. UM 439, van Zee et al. 1998) or a pronounced warp (e.g. NGC 2915, Elson et al. 2010).

Our galaxy sample includes BCDs from all these 4 classes. As we described in Sect. 6.5, NGC 4214 and NGC 4163 have several nearby companions belonging to the CVn I cloud and, thus, fit into class 1. Grocholski et al. (2008) argued that NGC 1560 and UGCA 290 may form a pair of galaxies in the IC 432 group similar to the LMC and the SMC in the Local Group; in this case, NGC 1569 would also belong to class 1. There may be more BCDs in this class, having galaxies at projected distances $D_{\rm p} \lesssim 200$ kpc and differences in their systemic velocities $\lesssim 300$ km s^{-1}, but the lack of accurate distance estimates for their potential companions prevents us from unambiguously classifying them (see Sect. 6.5). I Zw 18, NGC 4449, and NGC 2366 are probably undergoing a minor merger (see Lelli et al. 2012a, Martínez-Delgado et al. 2012, and Sect. 6.5,

respectively) and, thus, may belong to class 2. I Zw 36, UGC 6431, UGCA 290, and NGC 625 can be included in class 3, whereas UGC 4483, UGC 6456, UGC 9128, and SBS 1415+437 belong to class 4. NGC 6789 and NGC 5253 are somewhat intermediate between class 3 and 4, having $A \simeq 0.6$.

The observational evidence presented so far indicates that past and on-going interaction/accretion events play an important role in triggering the starburst in low-mass galaxies. Moreover, interaction/mergers between gas-rich dwarfs may provide the mechanism that forms the central concentration of mass observed in BCDs (see Lelli et al. 2012a,b and Chapter 5). Numerical simulations, indeed, indicate that interactions/mergers between gas-rich dwarfs may lead to an overall contraction of the disk and form a central mass concentration (e.g. Bekki 2008). However, to unambiguously identify galaxy interaction as the main triggering mechanism, one would need very deep optical observations (down to $\sim 29-30$ mag arcsec^{-2}) to search for stellar tidal features associated with the H I features, and/or for faint, low-surface-brightness companions. Several galaxies in our sample, indeed, show remarkably symmetric optical morphologies (down to $\sim$26 mag arcsec^{-2}), whereas the H I distribution is heavily pertured (see e.g. I Zw 36 in Fig. 6.9). In the case that stellar tidal features would still remain undetected by deep optical observations, the remaining possibility is that BCDs are directly accreting gas from the IGM. Cold flows of gas are predicted by ΛCDM models of galaxy formation (Kereš et al. 2005; Dekel & Birnboim 2006). In particular, Kereš et al. (2005) argued that these cold flows might still take place at $z \simeq 0$ in low-mass galaxies residing in low-density enviroments. As we discussed in Sect. 6.5, most BCDs in our sample inhabit similar environments as typical Irrs, such as galaxy groups and small associations. Thus, it is unclear why cosmological cold flows should be visible only in BCDs, unless they are highly stochastic and can rapidly trigger a central starburst by bringing large amounts of gas to the bottom of the potential well. It is also unclear what the relation would be between these cold flows and the central concentration of mass (luminous and/or dark). Three galaxies (NGC 1705, NGC 6789, and UGC 9128), however, *seem* very isolated and show relatively-regular optical morphologies down to $\mu \simeq 26$ R mag arcsec^{-2}. NGC 1705 shows a strong offset between the H I and stellar distribution, NGC 6789 has an anomalous H I extension to the West, while in UGC 9128 the optical and kinematical position angles differ by $\sim$30° (see Sect. 6.5 and Chapter 4). If the regular optical morphologies of these galaxies are confirmed by deeper optical images, they may represent cases of cold gas accretion in the nearby Universe.

6.7 Conclusions

We investigated the large-scale H I emission in a sample of 18 starbursting dwarf galaxies, using both new and archival data. We considered only galaxies that

have been resolved into single stars by HST observations, providing their recent SFHs and starburst timescales. Our main results can be summarized as follows.

1. Starbursting dwarfs display a broad, continuous range of H I morphologies. Several galaxies show heavily disturbed H I morphologies characterized by large-scale asymmetries, long filaments, and/or strong offsets between the stellar and H I distributions, whereas other galaxies show only minor asymmetries in the outer regions.

2. We defined the parameter A to quantify the H I asymmetry in the outer parts, and measured it for our sample of starbursting dwarfs and a control-sample of non-starbursting irregulars, drawn from the VLA-ANGST survey. We found that starbursting dwarfs generally have higher values of A than typical irregulars, suggesting that some external mechanism triggered the starburst.

3. We compared the values of A with the starburst properties. We found that galaxies hosting a "young" burst ($\lesssim$100 Myr) generally have more asymmetric H I morphologies than galaxies hosting an "old" one ($\gtrsim$100 Myr), further indicating that there is a close link between the outer, disturbed H I distribution and the central, recent star-formation. Galaxies hosting an "old" burst likely had enough time to partially regularize their outer H I distribution, since the "age" of the burst ($\sim$500 Myr) is comparable with the orbital time in the outer parts.

4. We investigated the nearby environment of the galaxies in our sample. Most of them have a potential perturber at a projected distance $\lesssim$ 200 kpc, thus the hypothesis of a past interaction cannot be excluded. Three galaxies (NGC 2366, NGC 4449, and I Zw 18) are probably undergoing a minor merger. Another three objects (NGC 1705, NGC 6789, and UGC 9128), instead, seem very isolated and show regular optical morphologies down to $\mu \simeq 26$ R mag arcsec^{-2}, thus they *may* represent cases of cold gas accretion in the nearby Universe.

Acknowledgements

We are grateful to Renzo Sancisi for sharing his valuable insights with us. We thank Juergen Ott for useful correspondence about the VLA-ANGST data, and Kristen McQuinn for sharing information about the stellar populations of the ANGST galaxies. We are grateful to Martin Vogelaar for implementing a special version of the Gipsy task "Visions". We also thank Ed Elson, Deidre Hunter, and Angel R. López-Sánchez for providing us with the H I data of NGC 1705, NGC 4449, and NGC 5253, respectively. Finally, we thank the members of the WHISP, THINGS, LITTLE-THINGS, and VLA-ANGST projects for having made the H I data publicly available. FL acknowledges the Ubbo Emmius

bursary program of the University of Groningen and the Leids Kerkhoven-Bosscha Fund. FF acknowledges financial support from PRIN MIUR 2010-2011, project "The Chemical and Dynamical Evolution of the Milky Way and Local Group Galaxies", prot. 2010LY5N2T.

Appendix 6.A The noise in a total H I map

In their appendix A, Verheijen & Sancisi (2001) describe how to calculate the noise in a total H I map obtained using a mask on an hanning-tapered datacube, in which all the channel maps are kept during the analysis. Here, we derive similar formulae that can be used to construct signal-to-noise maps in 2 different cases: i) a uniform-tapered datacube, as it is the case for the WHISP data and our new WRST and VLA observations; and ii) an online hanning-tapered datacube, in which half of the channel maps are discarded during the observations, as it is the case for the THINGS/LITTLE-THINGS data and other archival VLA observations.

Uniform taper

If the observations are made using an uniform velocity taper, the noise σ^u in two channel maps will be independent. When N uniform-tapered channel maps are added at the spatial position (x, y), the noise σ^u_N in the total H I map will increase by a factor $\sqrt{N}$, thus $\sigma^u_N(x, y) = \sqrt{N(x, y)}\sigma^u$. However, before the channel maps are added to form a total H I map, the continuum emission is subtracted, introducing further noise in the channel maps. Here we assume that the continuum map C^u is constructed by averaging N_1 and N_2 line-free channel maps at the high and low velocity ends of the datacube, respectively. Thus, one has

$$C^u = \frac{1}{2}\left(\frac{1}{N_1}\sum_{j=1}^{N_1} U_j + \frac{1}{N_2}\sum_{j=1}^{N_2} U_j\right), \tag{6.A.1}$$

and the noise σ^u_C in the continuum map is given by

$$\sigma^u_C = \frac{1}{2}\sqrt{\frac{1}{N_1} + \frac{1}{N_2}}\sigma^u. \tag{6.A.2}$$

If U_i is the value of a pixel in the ith uniform-tapered channel map, the line-emission L^u_i is given by $L^u_i = U_i - C^u$ and the noise σ^{lu}_i in L^u_i is given by

$$\sigma^{lu}_i = \sqrt{1 + \frac{1}{4}\left(\frac{1}{N_1} + \frac{1}{N_2}\right)}\sigma^u \tag{6.A.3}$$

When N uniform-tapered and continuum-subtracted channel maps are added, the signal L^u_N at a position (x, y) of the total H I map is given by

$$L^u_N(x, y) = \sum_{j=1}^{N(x,y)} L^u_j = \sum_{j=1}^{N(x,y)} U_j - N(x, y) \times C \tag{6.A.4}$$

and the noise σ_N^{lu} is given by

$$\begin{aligned}\sigma_N^{lu}(x,y) &= \sqrt{N(x,y)\sigma^{u^2} + N(x,y)^2\sigma_C^{u^2}} = \\ &= \sqrt{1+\frac{N(x,y)}{4}\left(\frac{1}{N_1}+\frac{1}{N_2}\right)}\sqrt{N(x,y)}\sigma^u.\end{aligned} \tag{6.A.5}$$

Online hanning taper

If the observations are made using an hanning taper, the datacube is smoothed in velocity and the noise in two adjacent channel maps is no longer independent. When the online hanning smoothing option of the VLA is used, half of the channel maps are discarted. If U_i and O_i are, respectively, the values of a pixel in the ith uniform-tapered and online hanning-tapered channel maps, one has

$$\begin{aligned}O_i &= \frac{1}{4}U_{i-1} + \frac{1}{2}U_i + \frac{1}{4}U_{i+1}, \\ O_{i+1} &= \frac{1}{4}U_i + \frac{1}{2}U_{i+1} + \frac{1}{4}U_{i+2}, \\ O_{i+2} &= \frac{1}{4}U_{i+1} + \frac{1}{2}U_{i+2} + \frac{1}{4}U_{i+3},\end{aligned} \tag{6.A.6}$$

and the $i+1^{th}$ channel map is discarted during the observations. The remaining channel maps i^{th} and $i+2^{th}$ are *not* independent, because both contain a quarter of the emission U_{i+1}. Thus, when N online hanning-smoothed channel maps are added, the noise σ_N^o does not increase by a factor $\sqrt{N}$, but by a factor $\sqrt{N-\frac{3}{4}}\frac{4}{\sqrt{2}\sqrt{6}}$, as we show in the following. The noise σ^o in the online hanning smoothed channel maps is equal to $\frac{\sqrt{6}}{4}\sigma^u$ (see Verheijen & Sancisi 2001). The total signal O_N is given by

$$O_N = O_i + O_{i+2} + O_{i+4} + O_{i+6} + ... + O_{i+2(N-1)}. \tag{6.A.7}$$

Table 6.7 – Adding N online hanning-tapered channel maps.

Channel	U_{i-1}	U_i	U_{i+1}	U_{i+2}	U_{i+3}	...	U_{i+2N-3}	U_{i+2N-2}	U_{i+2N-1}
i	1/4	1/2	1/4						
$i+2$			1/4	1/2	1/4				
...					...	...	...		
$i+2N-2$							1/4	1/2	1/4
	1/4	1/2	1/2	1/2	1/2	...	1/2	1/2	1/4

As it is shown by Table 6.7, one has

$$O_N = \frac{1}{4}U_{i-1} + \frac{1}{2}U_i + \frac{1}{2}U_{i+1} + ... + \frac{1}{2}U_{i+2N-2} + \frac{1}{4}U_{i+2N-1}, \tag{6.A.8}$$

and the noise σ_N^o is given by

$$\begin{aligned}\sigma_{\mathrm{N}}^{\mathrm{o}} &= \sqrt{\left(\frac{1}{4}\right)^2 + \left(\frac{1}{2}\right)^2 (2N-2) + \left(\frac{1}{4}\right)^2}\,\sigma^u = \\ &= \frac{1}{\sqrt{2}}\sqrt{N-\frac{3}{4}}\sigma^u = \sqrt{N-\frac{3}{4}}\frac{4}{\sqrt{2}\sqrt{6}}\sigma^o.\end{aligned} \tag{6.A.9}$$

The continuum map C^o is now constructed by averaging N_1 and N_2 line-free channel maps at high and low velocity ends of the online hanning-tapered datacube, thus the noise σ_C^o in C^o is given by

$$\begin{aligned}\sigma_C^o &= \frac{1}{2\sqrt{2}}\sqrt{\frac{1}{N_1^2}\left(N_1-\frac{3}{4}\right)+\frac{1}{N_1^2}\left(N_2-\frac{3}{4}\right)}\sigma^u \\ &\equiv \frac{1}{\sqrt{2}}A\sigma^u = \frac{4}{\sqrt{2}\sqrt{6}}A\sigma^o\end{aligned} \tag{6.A.10}$$

The line-emission in the ith channel maps is given by $L_i^o = O_i - C^o$ and the noise in L_i^o is given by

$$\sigma_i^{lo} = \sqrt{1+\frac{4}{3}A^2}\sigma^o \tag{6.A.11}$$

When N online hanning-tapered and continuum-subtracted channel maps are added, the signal L_N^o at a position (x, y) of the total H I maps is given by

$$\begin{aligned}L_N^o(x,y) = &\frac{1}{4}U_{i-1} + \frac{1}{2}U_i + ... + \frac{1}{2}U_{i+2N-2} + \frac{1}{4}U_{i+2N-1} + \\ &- N(x,y)\times C^o\end{aligned} \tag{6.A.12}$$

and the noise σ_N^{lo} at (x, y) is given by

$$\sigma_N^{lo}(x,y) = \sqrt{N(x,y)-\frac{3}{4}+N^2(x,y)A^2}\frac{4}{\sqrt{2}\sqrt{6}}\sigma^o \tag{6.A.13}$$

Note that this equation differs by a factor $1/\sqrt{2}$ from the one given by Verheijen & Sancisi (2001), which is valid in the case that all the hanning-tapered channel maps are kept during the data analysis.

References

Annibali, F., Cignoni, M., Tosi, M., et al. 2013, ArXiv e-prints
Annibali, F., Greggio, L., Tosi, M., Aloisi, A., & Leitherer, C. 2003, AJ, 126, 2752
Ashley, T., Simpson, C. E., & Elmegreen, B. G. 2013, ArXiv e-prints
Baldwin, J. E., Lynden-Bell, D., & Sancisi, R. 1980, MNRAS, 193, 313
Bekki, K. 2008, MNRAS, 388, L10
Bekki, K. & Freeman, K. C. 2002, ApJL, 574, L21
Berg, D. A., Skillman, E. D., Marble, A. R., et al. 2012, ApJ, 754, 98
Binder, B., Williams, B. F., Eracleous, M., et al. 2011, ApJ, 737, 77
Bouchard, A., Prugniel, P., Koleva, M., & Sharina, M. 2010, A&A, 513, A54
Bravo-Alfaro, H., Brinks, E., Baker, A. J., Walter, F., & Kunth, D. 2004, AJ, 127, 264
Briggs, D. S. 1995, in Bulletin of the American Astronomical Society, Vol. 27, Bulletin of the American Astronomical Society, 1444–+
Campos-Aguilar, A. & Moles, M. 1991, A&A, 241, 358
Campos-Aguilar, A., Moles, M., & Masegosa, J. 1993, AJ, 106, 1784
Cannon, J. M., McClure-Griffiths, N. M., Skillman, E. D., & Côté, S. 2004, ApJ, 607, 274
Chengalur, J. N., Pustilnik, S. A., Martin, J., & Kniazev, A. Y. 2006, MNRAS, 371, 1849
Conselice, C. J. 2003, ApJS, 147, 1
Côté, S., Carignan, C., & Freeman, K. C. 2000, AJ, 120, 3027
Cote, S., Freeman, K. C., Carignan, C., & Quinn, P. J. 1997, AJ, 114, 1313
Cox, A. L., Sparke, L. S., Watson, A. M., & van Moorsel, G. 2001, AJ, 121, 692
Crone, M. M., Schulte-Ladbeck, R. E., Greggio, L., & Hopp, U. 2002, ApJ, 567, 258
Dalcanton, J. J., Williams, B. F., Seth, A. C., et al. 2009, ApJS, 183, 67
Dekel, A. & Birnboim, Y. 2006, MNRAS, 368, 2
del Río, M. S., Brinks, E., & Cepa, J. 2004, AJ, 128, 89
Drozdovsky, I. O., Schulte-Ladbeck, R. E., Hopp, U., Crone, M. M., & Greggio, L. 2001, ApJL, 551, L135
Ekta, Chengalur, J. N., & Pustilnik, S. A. 2006, MNRAS, 372, 853
Ekta, Chengalur, J. N., & Pustilnik, S. A. 2008, MNRAS, 391, 881
Ekta, B. & Chengalur, J. N. 2010, MNRAS, 403, 295
Ekta, B., Pustilnik, S. A., & Chengalur, J. N. 2009, MNRAS, 397, 963
Elmegreen, B. G., Zhang, H.-X., & Hunter, D. A. 2012, ApJ, 747, 105
Elson, E. C., de Blok, W. J. G., & Kraan-Korteweg, R. C. 2010, MNRAS, 404, 2061
Elson, E. C., de Blok, W. J. G., & Kraan-Korteweg, R. C. 2011, MNRAS, 415, 323
Elson, E. C., de Blok, W. J. G., & Kraan-Korteweg, R. C. 2013, MNRAS, 429, 2550

Evstigneeva, E. A., Drinkwater, M. J., Jurek, R., et al. 2007, MNRAS, 378, 1036
Ferrara, A. & Tolstoy, E. 2000, MNRAS, 313, 291
Firth, P., Evstigneeva, E. A., Jones, J. B., et al. 2006, MNRAS, 372, 1856
Gil de Paz, A., Madore, B. F., & Pevunova, O. 2003, ApJS, 147, 29
Grocholski, A. J., Aloisi, A., van der Marel, R. P., et al. 2008, ApJL, 686, L79
Guseva, N. G., Papaderos, P., Izotov, Y. I., et al. 2003, A&A, 407, 105
Holwerda, B. W., Pirzkal, N., de Blok, W. J. G., & Blyth, S. 2013, ArXiv e-prints
Holwerda, B. W., Pirzkal, N., de Blok, W. J. G., et al. 2011a, MNRAS, 416, 2437
Holwerda, B. W., Pirzkal, N., de Blok, W. J. G., et al. 2011b, MNRAS, 416, 2401
Holwerda, B. W., Pirzkal, N., de Blok, W. J. G., et al. 2011c, MNRAS, 416, 2415
Holwerda, B. W., Pirzkal, N., de Blok, W. J. G., & van Driel, W. 2011d, MNRAS, 416, 2447
Hunter, D. A. & Elmegreen, B. G. 2004, AJ, 128, 2170
Hunter, D. A., Ficut-Vicas, D., Ashley, T., et al. 2012, AJ, 144, 134
Hunter, D. A., Wilcots, E. M., van Woerden, H., Gallagher, J. S., & Kohle, S. 1998, ApJL, 495, L47
Iovino, A., Melnick, J., & Shaver, P. 1988, ApJL, 330, L17
Izotov, Y. I. & Thuan, T. X. 1999, ApJ, 511, 639
Johnson, M., Hunter, D. A., Oh, S.-H., et al. 2012, AJ, 144, 152
Kaisin, S. S. & Karachentsev, I. D. 2008, A&A, 479, 603
Kantharia, N. G., Ananthakrishnan, S., Nityananda, R., & Hota, A. 2005, A&A, 435, 483
Karachentsev, I. D. 2005, AJ, 129, 178
Karachentsev, I. D., Dolphin, A. E., Geisler, D., et al. 2002, A&A, 383, 125
Karachentsev, I. D., Karachentseva, V. E., Huchtmeier, W. K., & Makarov, D. I. 2004, AJ, 127, 2031
Karachentsev, I. D., Makarov, D. I., & Kaisina, E. I. 2013, AJ, 145, 101
Karachentsev, I. D., Sharina, M. E., Dolphin, A. E., et al. 2003, A&A, 398, 467
Kereš, D., Katz, N., Weinberg, D. H., & Davé, R. 2005, MNRAS, 363, 2
Kobulnicky, H. A. & Skillman, E. D. 1997, ApJ, 489, 636
Kovač, K., Oosterloo, T. A., & van der Hulst, J. M. 2009, MNRAS, 400, 743
Lauberts, A. & Valentijn, E. A. 1989, The surface photometry catalogue of the ESO-Uppsala galaxies
Lee, J. C., Salzer, J. J., Law, D. A., & Rosenberg, J. L. 2000, ApJ, 536, 606
Lelli, F., Verheijen, M., Fraternali, F., & Sancisi, R. 2012a, A&A, 537, A72
Lelli, F., Verheijen, M., Fraternali, F., & Sancisi, R. 2012b, A&A, 544, A145
López-Sánchez, Á. R. 2010, A&A, 521, A63
López-Sánchez, A. R., Koribalski, B., van Eymeren, J., et al. 2010, in

Astronomical Society of the Pacific Conference Series, Vol. 421, Galaxies in Isolation: Exploring Nature Versus Nurture, ed. L. Verdes-Montenegro, A. Del Olmo, & J. Sulentic, 65
López-Sánchez, Á. R., Koribalski, B. S., van Eymeren, J., et al. 2012, MNRAS, 419, 1051
Lotz, J. M., Primack, J., & Madau, P. 2004, AJ, 128, 163
Mac Low, M. & Ferrara, A. 1999, ApJ, 513, 142
Manthey, E. & Oosterloo, T. 2008, in American Institute of Physics Conference Series, Vol. 1035, The Evolution of Galaxies Through the Neutral Hydrogen Window, ed. R. Minchin & E. Momjian, 156–158
Martínez-Delgado, D., Romanowsky, A. J., Gabany, R. J., et al. 2012, ApJL, 748, L24
Mateo, M. L. 1998, ARA&A, 36, 435
Matthews, L. D. & Uson, J. M. 2008, AJ, 135, 291
Maurogordato, S., Proust, D., Cappi, A., Slezak, E., & Martin, J. M. 1997, A&AS, 123, 411
McQuinn, K. B. W., Skillman, E. D., Cannon, J. M., et al. 2010, ApJ, 721, 297
McQuinn, K. B. W., Skillman, E. D., Dalcanton, J. J., et al. 2012, ApJ, 759, 77
Méndez, D. I. & Esteban, C. 2000, A&A, 359, 493
Méndez, D. I., Esteban, C., & Balcells, M. 1999, AJ, 117, 1229
Meurer, G. R., Carignan, C., Beaulieu, S. F., & Freeman, K. C. 1996, AJ, 111, 1551
Meurer, G. R., Staveley-Smith, L., & Killeen, N. E. B. 1998, MNRAS, 300, 705
Noeske, K. G., Iglesias-Páramo, J., Vílchez, J. M., Papaderos, P., & Fricke, K. J. 2001, A&A, 371, 806
Noguchi, M. 1988, A&A, 201, 37
Noordermeer, E., van der Hulst, J. M., Sancisi, R., Swaters, R. A., & van Albada, T. S. 2005, A&A, 442, 137
Oh, S., de Blok, W. J. G., Walter, F., Brinks, E., & Kennicutt, R. C. 2008, AJ, 136, 2761
Ott, J., Stilp, A. M., Warren, S. R., et al. 2012, AJ, 144, 123
Papaderos, P., Izotov, Y. I., Thuan, T. X., et al. 2002, A&A, 393, 461
Pustilnik, S., Ugryumov, A. V., Lipovetsky, V. A., Thuan, T. X., & Guseva, N. 1995, ApJ, 443, 499
Pustilnik, S. A., Brinks, E., Thuan, T. X., Lipovetsky, V. A., & Izotov, Y. I. 2001a, AJ, 121, 1413
Pustilnik, S. A., Kniazev, A. Y., Lipovetsky, V. A., & Ugryumov, A. V. 2001b, A&A, 373, 24
Putman, M. E., Bureau, M., Mould, J. R., Staveley-Smith, L., & Freeman, K. C. 1998, AJ, 115, 2345
Salzer, J. J. 1989, ApJ, 347, 152
Sancisi, R., Fraternali, F., Oosterloo, T., & van der Hulst, T. 2008, A&ARv, 15, 189

Schulte-Ladbeck, R. E., Hopp, U., Greggio, L., & Crone, M. M. 2000, AJ, 120, 1713
Schulte-Ladbeck, R. E., Hopp, U., Greggio, L., Crone, M. M., & Drozdovsky, I. O. 2001, AJ, 121, 3007
Silk, J., Wyse, R. F. G., & Shields, G. A. 1987, ApJL, 322, L59
Simpson, C. E., Hunter, D. A., Nordgren, T. E., et al. 2011, AJ, 142, 82
Skillman, E. D., Côté, S., & Miller, B. W. 2003, AJ, 125, 593
Stil, J. M. & Israel, F. P. 1998, A&A, 337, 64
Stil, J. M. & Israel, F. P. 2002, A&A, 392, 473
Swaters, R. A. & Balcells, M. 2002, A&A, 390, 863
Swaters, R. A., van Albada, T. S., van der Hulst, J. M., & Sancisi, R. 2002, A&A, 390, 829
Taylor, C., Brinks, E., & Skillman, E. D. 1993, AJ, 105, 128
Taylor, C. L., Brinks, E., Grashuis, R. M., & Skillman, E. D. 1995, ApJS, 99, 427
Taylor, C. L., Thomas, D. L., Brinks, E., & Skillman, E. D. 1996, ApJS, 107, 143
Telles, E. & Maddox, S. 2000, MNRAS, 311, 307
Telles, E. & Terlevich, R. 1995, MNRAS, 275, 1
Thilker, D. A., Bianchi, L., Schiminovich, D., et al. 2010, ApJL, 714, L171
Thuan, T. X., Hibbard, J. E., & Lévrier, F. 2004, AJ, 128, 617
Thuan, T. X. & Izotov, Y. I. 2005, ApJS, 161, 240
Trentham, N., Tully, R. B., & Verheijen, M. A. W. 2001, MNRAS, 325, 385
van Zee, L., Salzer, J. J., & Skillman, E. D. 2001, AJ, 122, 121
van Zee, L., Skillman, E. D., & Salzer, J. J. 1998, AJ, 116, 1186
Verheijen, M. & Sancisi, R. 2001, A&A, 370, 765
Walter, F., Brinks, E., de Blok, W. J. G., et al. 2008, AJ, 136, 2563
Walter, F., Brinks, E., Duric, N., & Klein, U. 1997, AJ, 113, 2031
Weisz, D. R., Dalcanton, J. J., Williams, B. F., et al. 2011, ApJ, 739, 5